SANDIA REPORT

SAND2013-10271
Unlimited Release
Printed December 2013

LDRD Final Report: Mesoscale Modeling of Dynamic Loading of Heterogeneous Materials

Joshua Robbins, Remi Dingreville, Thomas E. Voth, and Mike Furnish

Prepared by
Sandia National Laboratories
Albuquerque, New Mexico 87185 and Livermore, California 94550

Sandia National Laboratories is a multi-program laboratory managed and operated by Sandia Corporation, a wholly owned subsidiary of Lockheed Martin Corporation, for the U.S. Department of Energy's National Nuclear Security Administration under contract DE-AC04-94AL85000.

Approved for public release; further dissemination unlimited.

Sandia National Laboratories

Issued by Sandia National Laboratories, operated for the United States Department of Energy by Sandia Corporation.

NOTICE: This report was prepared as an account of work sponsored by an agency of the United States Government. Neither the United States Government, nor any agency thereof, nor any of their employees, nor any of their contractors, subcontractors, or their employees, make any warranty, express or implied, or assume any legal liability or responsibility for the accuracy, completeness, or usefulness of any information, apparatus, product, or process disclosed, or represent that its use would not infringe privately owned rights. Reference herein to any specific commercial product, process, or service by trade name, trademark, manufacturer, or otherwise, does not necessarily constitute or imply its endorsement, recommendation, or favoring by the United States Government, any agency thereof, or any of their contractors or subcontractors. The views and opinions expressed herein do not necessarily state or reflect those of the United States Government, any agency thereof, or any of their contractors.

Printed in the United States of America. This report has been reproduced directly from the best available copy.

Available to DOE and DOE contractors from
U.S. Department of Energy
Office of Scientific and Technical Information
P.O. Box 62
Oak Ridge, TN 37831

Telephone: (865) 576-8401
Facsimile: (865) 576-5728
E-Mail: reports@adonis.osti.gov
Online ordering: http://www.osti.gov/bridge

Available to the public from
U.S. Department of Commerce
National Technical Information Service
5285 Port Royal Rd
Springfield, VA 22161

Telephone: (800) 553-6847
Facsimile: (703) 605-6900
E-Mail: orders@ntis.fedworld.gov
Online ordering: http://www.ntis.gov/help/ordermethods.asp?loc=7-4-0#online

SAND2013-10271
Unlimited Release
Printed December 2013

LDRD Final Report: Mesoscale Modeling of Dynamic Loading of Heterogeneous Materials

Joshua Robbins
Computational Shock and Multiphysics
jrobbin@sandia.gov

Remi Dingreville
Structural and Thermal Analysis
rdingre@sandia.gov

Thomas E. Voth
Computational Shock and Multiphysics
tevoth@sandia.gov

Michael D. Furnish
Dynamic Material Properties
mdfurni@sandia.gov

Abstract

Material response to dynamic loading is often dominated by microstructure (grain structure, porosity, inclusions, defects). An example critically important to Sandia's mission is dynamic strength of polycrystalline metals where heterogeneities lead to localization of deformation and loss of shear strength. Microstructural effects are of broad importance to the scientific community and several institutions within DoD and DOE; however, current models rely on inaccurate assumptions about mechanisms at the sub-continuum or mesoscale. Consequently, there is a critical need for accurate and robust methods for modeling heterogeneous material response at this lower length scale. This report summarizes work performed as part of an LDRD effort (FY11 to FY13; project number 151364) to meet these needs.

Acknowledgment

This work was funded under LDRD Project Number 151364 and Title ”Mesoscale Modeling of Dynamic Loading of Heterogeneous Materials”.

Contents

1 Introduction 9
2 Multi-resolution modeling of the dynamic loading of metal matrix composites 10
2.1 Direct Numerical Simulation of MMCs 12
2.2 Microcontinuum model of MMCs 17
2.3 Results and Discussion 21
2.4 Conclusions of Multi-Resolution Analysis 25
3 Dispersion due to microstructural features 27
3.1 Formulation of a nonlinear 1D micromorphic model 29
3.2 Dispersion relation, phase and group velocities 35
3.3 Discussion 40
3.4 Conclusions of Dispersion Analysis 44
4 Velocity Dispersion Experiments (DICE shots 242-244) 48
4.1 Configuration 48
4.2 Shot Details 50
4.3 Results 52
4.4 Conclusions of Experimental Work 53
References 55

Appendix

A Derivation of the fourth order equation of motion 64

Figures

1 Typical discretization of Al/SiC MMC. Longitudinal and lateral dimensions are 2.0 and 0.5 mm, respectively, and the microstructure is periodic with mesh resolution of 2.5μm. Aluminum matrix is semi-transparent, and SiC reinforcement is opaque. 15
2 Comparison of predicted velocity profiles for pulse loading. 16
3 Comparison of predicted velocity profiles for pulse loading. Cut planes are located at the peak of the pulse. 17
4 Schematic of a layered medium used for calibration. 21
5 Comparison of predicted velocity profiles between DNS and the microcontinuum model for a 1D layered Al/SiC composite in the elastic regime. (a) For a Gaussian input used for initial calibration (b) for a short pulse loading (c) for a long pulse loading (d) for an impact loading. 22
6 Comparison of predicted velocity profiles between DNS and the microcontinuum model for a 1D layered Al/SiC composite in the elasto-plastic regime. (a) For a Gaussian input pulse (b) for a short pulse loading (c) for a long pulse loading (d) for an impact loading. 23

7 Comparison of predicted velocity profiles between DNS and the microcontinuum model for a 3D particulate-reinforced Al/SiC MMC in the elastoplastic regime. The profiles shown of the DNS results are the average of three random microstructural realizations and include an upper and lower envelop that shows the standard deviation in velocity on the transverse plane at the given position. (a) For a Gaussian input pulse with a volume fraction of SiC of 5% (b) for a long pulse loading with a volume fraction of SiC of 5% (c) for a Gaussian input pulse with a volume fraction of SiC of 10% (b) for a long pulse loading with a volume fraction of SiC of 10% 24

8 $\bar{\gamma}$ is defined in the $\left(\gamma_{0\mu} - \beta_{0\mu}\right)$ space between the solid lines. 34

9 Dispersion relation for a hardening microstructured material following the equation of motion (40) with parameters $\gamma_\mu = 0.6$, $\gamma_{0\mu} = 1.6$, $\beta_{0\mu} = 1.3$, $\rho_\mu = 0.5$, $h_0 = 1.5$, $h_\mu = 3.0$ and $\varepsilon_\ell = 2.0$. Results illustrated in this figure are compared to the linear elastic case of equation (63) [26] for the same parameters. 37

10 (a) Phase velocity−frequency relation and (b) Phase velocity−wave number relation for a hardening microstructured material using the parameters provided in Figure 9. 38

11 (a) Phase velocity−frequency relation and (b) phase velocity−wave number relation for a hardening microstructured material using the parameters provided in Figure 9 for various microstructural length scales ε_ℓ. Results are normalized by the phase velocity $\gamma_{\pi,0}$ when the characteristic microstructural length scale is infinitely small (i.e. microstructural effect can be neglected). Solid lines denote the acoustic branch, dotted lines denote the optical branch. Square symbols represent the phase velocity for $\varepsilon_\ell = 0.75$, round symbols represent the phase velocity for $\varepsilon_\ell = 1.5$, triangle symbols represent the phase velocity for $\varepsilon_\ell = 3.0$, and diamond symbols represent the phase velocity for $\varepsilon_\ell = 6.0$. 39

12 (a) Group velocity−frequency relation and (b) Group velocity−wave number relation for a hardening microstructured material using the parameters provided in Figure 9. 40

13 (a) Group velocity−frequency relation and (b) group velocity−wave number relation for a hardening microstructured material using the parameters provided in Figure 9 for various microstructural length scales ε_ℓ. Results are normalized by the group velocity $\gamma_{g,0}$ when the characteristic microstructural length scale is infinitely small (i.e. microstructural effect can be neglected). Solid lines denote the acoustic branch, dotted lines denote the optical branch. Square symbols represent the phase velocity for $\varepsilon_\ell = 0.75$, round symbols represent the phase velocity for $\varepsilon_\ell = 1.5$, triangle symbols represent the phase velocity for $\varepsilon_\ell = 3.0$, and diamond symbols represent the phase velocity for $\varepsilon_\ell = 6.0$. 41

14 Impact of the macro-/microscopic materials constants on (a) dispersion relation, (b) phase velocity−wave number relation and (c) group velocity−wave number relation. Solid lines denote the acoustic branch, dotted lines the optical branch. Parameters common to all cases are $\gamma_\mu = 0.6$, $\rho_\mu = 0.5$ and $\varepsilon_\ell = 2.0$. The macro-/micro- hardening parameters (h_0/h_μ), coupling term ($\gamma_{0\mu}$) and micro-elasticity scaling factor ($\beta_{0\mu}$) are annotated for each case. 46

15 Comparison between a hardening microstructured material model and a gradient-dependent hardening material [101] for (a) Dispersion relation, (b) phase velocity−wave number relation, and (c) group velocity−wave number relation. Parameters used for the micromorphic hardening model are adapted from [101] such that $\gamma_\mu = 2$, $\rho_\mu = 1$, $\gamma_{0\mu} = 0.086$, $\beta_{0\mu} = 0.9$, $h_0 = -1.5$ and $h_\mu = 2.0$ and $\varepsilon_\ell = 2.0$. Parameters for the gradient dependent model are $h_0 = -1.5$, $\varepsilon_\ell = 2.0$ and $c_s = 1.6$. 47
16 General concept for DICE gas gun shots 242-244. 48
17 Velocity field from copper impacting copper bicrystal windowed by Z-cut quartz (DICE gas gun shot 199). 49
18 Padded transforms for simulated copper experiment with a variety of sliding FFT window widths, taken at the time noted on the synthetic trace. 50
19 . Shot 242 hardware. (a) Overall, (b) PDV probe holder, (c) nosetip with PMMA under copper (not used), (d) nosetip with aluminum under copper (used). 51
20 Padded transforms for DICE gas gun shot 243 (probe 1 data). Two different times are analyzed, with various FFT window widths. 52
21 Padded transforms for Al experiment, flat plateau and plateau with noted velocity dispersion 53

Tables

1 Elastic and viscoplastic parameters for Al matrix. 14

1 Introduction

A mesoscale modeling capability would serve two essential roles. The first is to simulate in full detail the response of polycrystalline material to dynamic loading. In this case, the microstructural details appear explicitly in the simulation. This approach is computationally expensive (days on a supercomputer), but provides direct insight into the microstructural origins of material response. The second role, with potentially broader impact, is to inform lightweight (minutes on a desktop computer) continuum models with information from mesoscale simulations. At longer length scales, where Direct Numerical Simulation (DNS) of microstructural effects is not computationally feasible, ”upscaling” techniques are a proven approach. Unfortunately, these methods typically assume static equilibrium, making them inappropriate for our applications. Further, current upscaling methods do not leverage statistical information about material response made available through mesoscale calculations. This project addressed these problems using Sandia's unique computational capabilities and codes to perform DNS of a number of microstructure realizations. Results were then used to inform dynamic upscaling models.

This report is organized as follows. Chapter one presents the dynamic upscaling approach in the context of metal matrix composites. Chapter two is a mathematical treatment of the dispersion and stability behavior of the micromorphic continuum method described in chapter one. Finally, chapter three discusses experimental work that was done for purposes of model validation.

2 Multi-resolution modeling of the dynamic loading of metal matrix composites

Metal matrix composites (MMCs) are produced by combining a base metal (such as Al or Ti) or a metallic alloy (such as Ni alloys) with another phase (often non-metallic) in order to create a novel material with improved mechanical performance compared to conventional materials and to reduce life-cycle costs through enhanced thermomechanical stability and weight reduction [32, 85, 86]. MMCs are generally categorized by the characteristics of their reinforcement: particle-reinforced MMCs (e.g. SiC or B_4C), short fiber- or whisker-reinforced MMCs (e.g. Al_2O_3), and fiber or layered MMCs (e.g. C or W). Motivated by technical challenges in processing such composites and tailorability of their properties, and due to the wide range of applications of these materials in advanced military systems (e.g. light-weight armor materials) and in the automotive and aerospace industries (e.g. impact shields, crash-tolerant structures) for example, MMCs and their thermomechanical performance have been the subject of much research in the late 1980s and early 1990s[20, 19, 70, 100, 73, 74, 24].

This class of materials is often subjected to high strain rate deformation, such as in the case of penetration of a projectile in an armor or the impact of an object on aerospace structures, and while showing good performance under such conditions, the mechanical behavior of MMCs varies significantly under rapid straining as compared to quasi-static loading. This behavior is often dominated by underlying microstructural features (grain structure, porosity, shape and spatial distribution of reinforcements, volume fraction of reinforcements) [58, 110, 57, 121, 71]. However, despite the great interest in MMCs, and considerable research into the effects of reinforcement type and volume fraction on macroscopic properties such as stiffness, ductility, wear resistance, or thermal conductivity, fewer studies have been conducted to examine the effects of those microstructural details on their dynamic loading behavior [49, 71, 103, 107]. The most common and versatile experimental techniques for materials research and characterization under high strain rate conditions are uniaxial in character, e.g., high velocity plate impact and magnetic pulse loading. The assumption of a uniaxial strain condition is valid at the macroscale, but at the length scale of the microstructure the deformation state is fully three dimensional [5]. Further, the effects of microstructural heterogeneities on the dynamic response of MMCs are particularly pronounced when the scale of the deformation is of the order of the material heterogeneities which is often the case in dynamic uniaxial experiments. Consequently, there is a critical need for accurate and robust methods for modeling heterogeneous material response at this lower length scale that can account for microstructural effects. Inspired by the work done by Liu and coworkers [111, 79], the present manuscript introduces a multi-resolution modeling framework to investigate the dynamic behavior of uniaxially loaded heterogeneous materials, MMCs in particular, by explicitly accounting for the microstructural features (both in the matrix and reinforcements) that influence the dynamic response.

A number of theoretical and numerical investigations have been performed mostly with the intent of predicting the stiffness and strength of a given composite given the properties of the matrix and reinforcement phase [21, 90, 71]. Analytical studies of the high strain rate deformation of particle reinforced MMCs are based on classical micromechanics schemes and homogenization

models (such as mixture models, Mori Tanaka or Hashin-Strickman schemes, etc.). For example, Bao and coworkers [7] carried out a micromechanics study to look at the effect of the volume fraction of inclusions on the strain rate dependence of the plastic flow behavior of Al/Al_2O_3 composites. More recently, Grujicic and coworkers [48] used a dynamic mixture model in order to investigate the propagation of structured waves within Al/SiC MMCs. Conventional numerical modeling of MMCs is typically conducted at the continuum scale by considering a unit cell model containing a single or multiple idealized reinforcement particle(s) such as a fiber (in the shape of an ellipsoid), a whisker (in the shape of a cylinder) or a particle (idealized as a sphere) embedded in a homogeneous host matrix via computational micromechanics [71, 10, 99, 124, 103, 107]. Li and Ramesh [71] for example performed a parametric study of the influence of particle volume, shape and aspect ratio on the behavior of particle-reinforced MMCs at high strain by using an axisymmetric unit cell model with particles treated as elastic ellipsoids or cylinders embedded in an homogeneous visco-plastic matrix. While the simplifications of the microstructural features in these unit cell models may help in reducing the simulation complexity, these models fail to capture the microstructural complexities associated with MMCs' constitutive components such as the inhomogeneous spatial distributions of particles, their irregular morphology, but also the crystallographic texture and inhomogeneous microstructure (grain size and morphology) of the host matrix itself. Accurate predictions and further understanding of the dynamic behavior for this type of material require an approach which explicitly accounts for realistic microstructures of these composites. For example, Chawla and co-workers [15, 16, 118] took a step in that direction by developing microstructure-based finite element techniques and importing experimentally characterized reinforcements (by serial sectioning, X-ray tomography or holotomography for example) within a numerical unit-cell framework to study failure mechanisms of MMCs.

Predicting microstructure-property relationships for the dynamic behavior of MMC materials via direct simulation of its underlying microstructure remains a difficult goal to reach due to the massive disparities in length and time scales. In this paper, we present a multi-resolution modeling capability for studying the nonlinear planar wave propagation in heterogeneous materials such as MMCs. This framework is based on (i) mesoscale direct numerical simulations (DNS) and (ii) an upscaled microcontinuum model. In this paper, the term *direct numerical simulation*, or DNS, refers to simulations in which the microstructural topology is explicitly resolved in the spatial discretization. This does not imply that the simulations are considered to be exact solutions to the physical problem, only that an approximation of the microstructure is modeled directly. The mesoscale DNS paradigm used in this work explicitly accounts for microstructural features (grain morphology and crystallographic texture of the matrix, morphology and spatial distribution of the reinforcements) and is based on a combination of a crystal plasticity formulation and Johnson–Holmquist model. Non-uniformity of the wave propagating through MMCs is resolved spatially and temporally through these simulations. Results from the mesoscale DNS are then used to inform a microcontinuum model which introduces richer kinematics to implicitly account for the above mentioned microstructural features without explicitly modeling them and with far fewer total degrees of freedom than the DNS. The motivation of such an approach is to develop novel multi-resolution continuum models of MMCs and relate their microstructure to their structural dynamic performance in a single framework. A quantitative comparison of the reduced degrees of freedom model against DNS is performed and enables us to draw conclusions on the predictive capability of the microcontinuum model compared to fully resolved models to study the dynamic

response of heterogeneous materials.

The manuscript is organized as follows. Section 2 introduces the details of the DNS model used presently. Section 3 describes the details of the microcontinuum model and briefly details the upscaling method between the results obtained from the mesoscale DNS and the microcontinuum model. As an illustration, this work focuses on a prototypical MMC system consisting of an aluminum polycrystalline matrix reinforced with SiC particulates. Section 4 provides a discussion on the main findings of the work for various MMCs (layered and particle reinforced) and recommendations for future investigations.

2.1 Direct Numerical Simulation of MMCs

In order to understand and study the dynamic behavior of MMCs, the construction of the multi-resolution continuum model starts at the microstructural level, by treating the material deformation of the MMC matrix with a standard crystal plasticity rate-dependent formulation [98], while the particle reinforcements are modeled through a Johnson–Holmquist (JH-1) model [60].

The foundations of the constitutive model for the MMC matrix assume that the elasto-visco-plastic response of single crystals is dominated by slip deformation mechanisms. Others mechanisms such as twinning, grain boundary sliding or diffusion are not considered. The total deformation of a single crystal consists of a plastic deformation, elastic lattice rotations and rigid body rotations. The single crystal kinematics is described by a multiplicative decomposition of the total deformation gradient $\mathbf{F}$ into a plastic component, $\mathbf{F}^{\text{plast}}$, representative of the intervening motion of dislocations on active slip systems leaving the crystal lattice unchanged, and an elastic component, $\mathbf{F}^{\text{elast}}$, depicting the rotation and elastic stretching of the matrix lattice. For isothermal conditions we have,

$$\mathbf{F} = \mathbf{F}^{\text{plast}} \cdot \mathbf{F}^{\text{elast}} \ . \tag{1}$$

Since the dynamic behavior of the polycrystalline matrix is of importance, a rate-form expression of the deformation is used to express the kinematics of the crystalline solid from the kinematic decomposition. The velocity gradient $\mathbf{L}$ in the current configuration can be written as,

$$\mathbf{L} = \dot{\mathbf{F}} \cdot \mathbf{F}^{-1} \ , \tag{2}$$

where $\dot{\mathbf{F}}$ is the rate of total deformation gradient. Subsequently, the velocity gradient $\mathbf{L}$ can be additively decomposed into its elastic $\mathbf{L}^{\text{elast}}$ and plastic $\mathbf{L}^{\text{plast}}$ counterparts. The plastic velocity gradient $\mathbf{L}^{\text{plast}}$ is assumed to be solely the result of crystallographic slip over S potentially active slip systems such that it corresponds to the sum of the plastic shearing rate $\dot{\gamma}^{\alpha}$ on S number of activated slip systems α [54, 4],

$$\mathbf{L}^{\text{plast}} = \sum_{\alpha=1}^{S} \dot{\gamma}^{\alpha} \bar{\mathbf{m}}^{\alpha} \otimes \bar{\mathbf{s}}^{\alpha} \ , \tag{3}$$

where plastic velocity gradient is resulting from the dyadic product of the crystallographic slip direction unit vector $\bar{\mathbf{m}}^{\alpha}$ and the slip plane normal unit vector $\bar{\mathbf{s}}^{\alpha}$ in the intermediate configuration.

The rate of plastic deformation gradient $\dot{\mathbf{F}}^{\text{plast}}$ resulting from crystal slip is governed by,

$$\dot{\mathbf{F}}^{\text{plast}} = \mathbf{L}^{\text{plast}} \cdot \mathbf{F}^{\text{plast}} \ . \tag{4}$$

A classical Hookean law gives the constitutive stress-strain relation under isothermal conditions such as,

$$\boldsymbol{\sigma}^{\text{PK2}} = \mathbb{C} : \mathbf{E}^{\text{elast}} \ , \tag{5}$$

$$\text{with} \quad \mathbf{E}^{\text{elast}} = \frac{1}{2}\left(\mathbf{F}^{\text{elast}^{\text{T}}} \cdot \mathbf{F}^{\text{elast}} - \mathbf{I}\right) \ , \tag{6}$$

where $\boldsymbol{\sigma}^{\text{PK2}}$ is the second Piola-Kirchoff stress tensor, $\mathbf{E}^{\text{elast}}$ is the Green-Lagrange tensorial elastic strain measure, $\mathbb{C}$ is the anisotropic fourth order elastic stiffness tensor, and $\mathbf{I}$ the second order identity tensor. The Cauchy stress tensor $\boldsymbol{\sigma}$ is related to the second Piola-Kirchoff stress tensor through [98],

$$\boldsymbol{\sigma} = \left[\det\left(\mathbf{F}^{\text{elast}}\right)\right]^{-1} \mathbf{F}^{\text{elast}} \cdot \boldsymbol{\sigma}^{\text{PK2}} \cdot \mathbf{F}^{\text{elast}^{\text{T}}} \ . \tag{7}$$

The resolved shear stress τ^{α} on slip system α is defined as,

$$\tau^{\alpha} = \boldsymbol{\sigma} : \left(\bar{\mathbf{m}}^{\alpha} \otimes \bar{\mathbf{s}}^{\alpha}\right) \ . \tag{8}$$

The flow and evolutionary equations describing the behavior of each individual slip system completes the formulation. The kinetic equation used for the crystallographic slip rate $\dot{\gamma}^{\alpha}$ follows a power law visco-plastic flow rule [56] such that,

$$\dot{\gamma}^{\alpha} = \dot{\gamma}_0 \left|\frac{\tau^{\alpha}}{\tau^{\alpha}_{\text{CRSS}}}\right|^{1/m} \text{sgn}\left(\tau^{\alpha}\right) \ , \tag{9}$$

where $\dot{\gamma}_0$ is the reference shearing rate, m is the rate sensitivity, and $\left(\tau^{\alpha}, \tau^{\alpha}_{\text{CRSS}}\right)$ are the resolved shear stress and total slip resistance (or critical resolved shear stress), respectively, on slip system α. The sign of the resolved shear stress $\text{sgn}\left(\tau^{\alpha}\right)$ accounts for either positive or negative slip on the system. Hardening of the slip systems assumes that dislocations act as obstacles to dislocation motion and contribute to the total slip resistance according to the Taylor equation [106]. The evolution of the overall resistance to slip, $\tau^{\alpha}_{\text{CRSS}}$, is given by

$$\tau^{\alpha}_{\text{CRSS}} = \lambda G_{[110]} b \sqrt{\rho^{\alpha}} \ , \tag{10}$$

where λ is a statistical coefficient accounting for the deviation from regular spatial arrangements of dislocations, b is the magnitude of the Burgers vector, ρ^{α} is the forest dislocation density for a given slip system α, and $G_{[110]}$ is the shear modulus on the $[110]$ plane. Note that the bulk shear modulus G is instead commonly used in the literature. However, at the grain level, the directional shear modulus seems a better choice due to the local anisotropy of the material. The evolution of the dislocation density is based on the phenomenological approach proposed by Kocks [64] and Mecking and Kocks[80] where dislocation sources and sinks are considered:

$$\frac{d\rho^{\alpha}}{d\gamma^{\alpha}} = h_1^{\text{KM}} \sqrt{\rho^{\alpha}} - h_2^{\text{KM}} \rho^{\alpha} \ , \tag{11}$$

where γ^{α} is the accumulated slip on the slip system α, and $\left(h_1^{\mathrm{KM}}, h_2^{\mathrm{KM}}\right)$ are material hardening parameters. The first term reflects that dislocation storage is inversely proportional to the dislocation mean free path, while the second hardening term describes the annihilation and cross-slip of dislocations. Finally, it should be mentioned that the focus of this work is on developing multi-resolution schemes to study the dynamic behavior of heterogeneous materials, rather than the physical models themselves. In other words, the aforementioned flow rule and hardening model are targeted at providing some simple features associated with the hardening of the matrix materials. The elastic constants and hardening parameters introduced in the constitutive model of the section described above are listed in Table 1.

Property	**Symbol**	**Value**
Elastic modulus	$\mathbb{C}_{11}$	108.2 GPa
Elastic modulus	$\mathbb{C}_{12}$	61.3 GPa
Elastic modulus	$\mathbb{C}_{44}$	28.5 GPa
Rate sensitivity	m	0.02
Reference shearing rate	$\dot{\gamma}_0$	20 s^{-1}
Magnitude of the Burgers vector	b	0.286 nm
Initial CRSS	$\tau^{\alpha}_{CRSS,0}$	45.0 MPa
Scaling factor	λ	0.5
Taylor hardening parameter	h_1^{KM}	$1.07 \times 10^8 \mathrm{m}^{-1}$
Taylor hardening parameter	h_2^{KM}	27.97

Table 1. Elastic and viscoplastic parameters for Al matrix.

The Johnson–Holmquist model [60] is used to describe the SiC particulates behavior. This model incorporates a strength response that possesses both a rate and pressure dependence and, even though this is not the focus of the present study, this model has features that makes it possible to examine the effects of fracture and imperfect interface on loading spreading through a damage parameter D. The rate dependence of the strength model reads,

$$\sigma = \sigma_0 \left(1 + c_1^{\mathrm{JH}} \ln \dot{\varepsilon}^*\right) \ , \tag{12}$$

where $\dot{\varepsilon}^* = \dot{\varepsilon}^{\mathrm{plast}} / \dot{\varepsilon}_0$ with ε_0 being a reference strain and $\varepsilon^{\mathrm{plast}}$ being the equivalent plastic strain, σ_0 is the material strength at $\dot{\varepsilon}^* = 1$ and c_1^{JH} is a material constant. The pressure dependent strength for intact $(D = 0)$ or partially damaged $(D < 1)$ material is given by a bilinear relationship in the pressure/strength space from points $(P = -P_T, \sigma = 0)$ to $(P = P_1, \sigma = S_1)$ and from $(P = P_1, \sigma = S_1)$ to $(P = P_2, \sigma = S_2)$ followed by a constant strength. The pressure dependence for fully damaged $(D = 1)$ material is given by a linear relation in the pressure/strength space from $\sigma = 0$ to $\sigma = S_3$ with a slope of c_1^{JH} followed by a constant strength.

The definition of the damage model describes the fracture behavior of the SiC reinforcements in which the degree of damage is characterized by a scalar metric D which varies between 0 (no damage) and 1 (complete damage). D is defined by,

$$D = \frac{\varepsilon^{\mathrm{plast}}}{\varepsilon^{\mathrm{frac}}} \ , \tag{13}$$

where $\varepsilon^{\text{frac}}$ is the equivalent plastic strain to fracture.

The Mie-Grüneisen equation of state for the volumetric response in the Johnson–Holmquist model is calculated using,

$$P = k_1^{\text{JH}}\mu + k_2^{\text{JH}}\mu^2 + k_3^{\text{JH}}\mu^3 \ , \tag{14}$$

where $\left(k_1^{\text{JH}}, k_2^{\text{JH}}, k_3^{\text{JH}}\right)$ are material constants, and $\mu = V_0/V - 1$ with V_0 and V being the initial and current specific volume respectively. The material parameters used in Johnson–Holmquist model are taken from Table 3 in Robbins et al. [97].

A set of different realizations of periodic three-dimensional (3D) representative microstructures containing Al grains and a given volume fraction of SiC particulate reinforcements was used for the DNS. A typical representative microstructure, illustrated in Figure 1, was obtained by means of a Voronoi tessalation. Dimensions of the representative volume element (RVE) in physical space is 2.0mm $\times$ 0.5mm $\times$ 0.5mm resulting in a average grain size of 65 μm and an average reinforcement size of 45 μm. RVEs containing 5% and 10% volume fraction of SiC particulates have been generated and simulated. For each representative microstructure, the crystallographic orientations assigned to each grain in the host matrix is allocated randomly while perfect bonding between the SiC particulates and Al grains is assumed. The typical mesh for the representative MMC microstructure, selected after a mesh convergence study, comprises an average of 32 million elements which is equivalent to a 2.5μm mesh resolution.

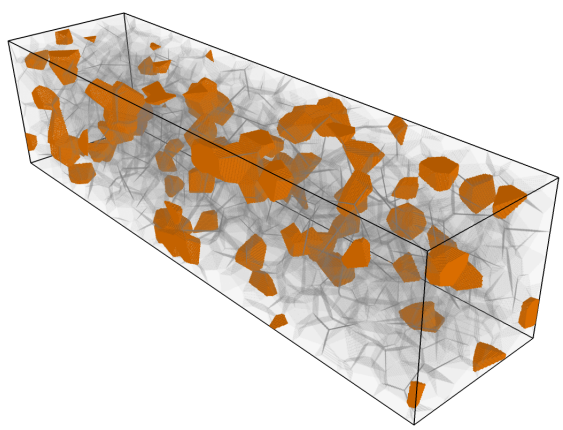

Figure 1. Typical discretization of Al/SiC MMC. Longitudinal and lateral dimensions are 2.0 and 0.5 mm, respectively, and the microstructure is periodic with mesh resolution of 2.5μm. Aluminum matrix is semi-transparent, and SiC reinforcement is opaque.

This DNS model for MMCs was implemented into Sandia's arbitrary eulerian lagrangian (ALE) massively parallel ALEGRA code [76, 75] and applied to model the dynamic hardening in particle-reinforced MMCs. The ALEGRA framework was used in a pure Lagrangian mode and

employs a finite element spatial discretization and an explicit central-difference stepping method in time. The simulations use eight node, uniform strain, (hexahedral) 3D isoparametric elements. Hourglass control is used to manage zero energy modes associated with the uniform strain element. Further details on the formulation of the ALEGRA framework are provided in the technical report by Love and Wong [76]. A set of 12 different 3D calculations were conducted using 1e4 processor-hours each. Velocity boundary conditions were prescribed as a Gaussian rightward compressive moving pulse of an approximate duration of 200 ns with a half height width of 65 ns at the left end side of the microstructure and with a magnitude of 200 m/s. The lateral sides of the microstructure have periodic boundary conditions. Typical results are presented in Figure 2 for a microstructure containing 5% of SiC particulates. The input pulse results in a compressive stress wave moving from left to right in the microstructure which reflects off the free surface after approximately 400 ns producing a release wave. Figure 2 shows grain-scale contour plots of longitudinal velocity at various stages of the wave propagating through the microstructure with sharp contrast between the Al matrix and SiC inclusions. As further illustrated in Figure 3 which shows the velocity on sample cross-sections, spatial variation in the velocity field is produced by the heterogeneity of the material resulting a decidedly multi-axial strain state at this length scale.

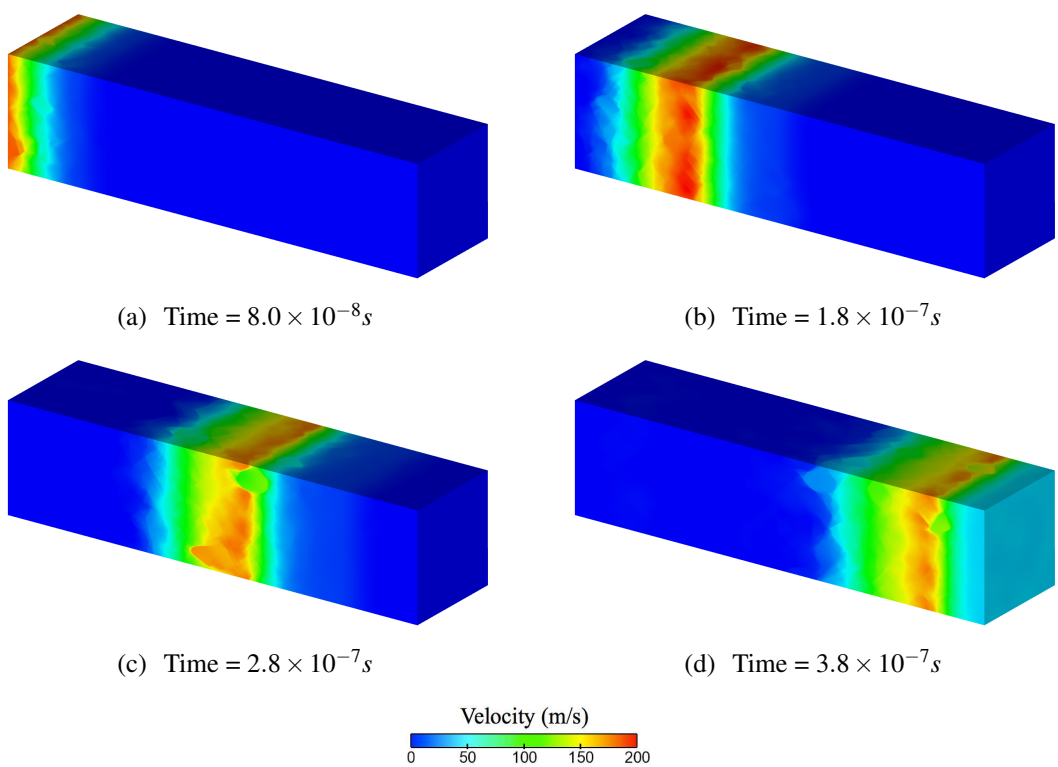

(a) Time = $8.0 \times 10^{-8} s$

(b) Time = $1.8 \times 10^{-7} s$

(c) Time = $2.8 \times 10^{-7} s$

(d) Time = $3.8 \times 10^{-7} s$

Figure 2. Comparison of predicted velocity profiles for pulse loading.

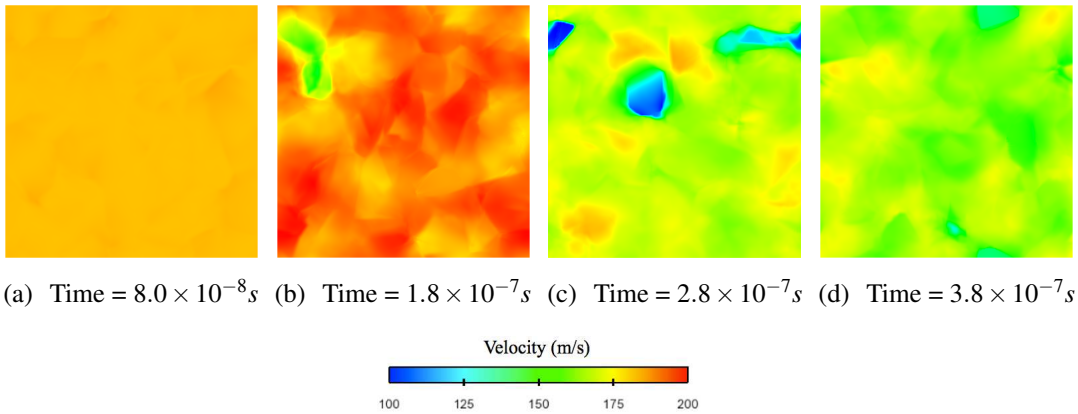

(a) Time = $8.0 \times 10^{-8} s$ (b) Time = $1.8 \times 10^{-7} s$ (c) Time = $2.8 \times 10^{-7} s$ (d) Time = $3.8 \times 10^{-7} s$

Figure 3. Comparison of predicted velocity profiles for pulse loading. Cut planes are located at the peak of the pulse.

2.2 Microcontinuum model of MMCs

Multiresolution continuum modeling

In an effort to bypass the limitations of computational speed associated with DNS while retaining microstructural effects, the second step of the construction of the multi-resolution continuum model is to pursue the development of an upscaling method informed with details from the mesoscale simulations. Incorporating some effects of characteristic microstructural features of the materials into constitutive modeling is possible via the mechanics of generalized continua. The goal is to endow the continuum with additional degrees of freedom that are supposedly independent from the usual translational degrees of freedom and representative of the microstructure [33]. The article by Germain [38] and the book by Eringen[29] provide detailed reviews of the mechanics of higher order continua. In a microcontinuum model, the underlying microstructure at any material point of the continuum can rotate and deform. In this context, if we consider a continuum $\mathscr{D}$ as a deformable continuous distribution of material points, each of them is geometrically represented by a point M and characterized kinematically by a macroscopic and microscopic displacement field. The macroscopic displacement field $\mathbf{u}$ is defined as $u_i = x_i - X_i, i = 1 \ldots 3$, where x_i and X_i are the coordinates of a material point in the deformed and undeformed reference coordinate system, respectively. The microdisplacement $\mathbf{u}'$ is defined by its components $u'_i = x'_i - X'_i$, where x'_i are the coordinates of a point M' belonging to a microvolume $\Omega(M)$ around M and measured from the center of mass M of this microvolume.

Following the development of Mindlin [83], the balance equations for a microstructured mate-

rial can be expressed as,

$$\nabla \cdot (\boldsymbol{\sigma} + \boldsymbol{\tau}) = \rho \ddot{\mathbf{u}} \quad \text{in } \mathscr{D} \,, \tag{15}$$

$$\nabla \cdot \boldsymbol{\mu} + \boldsymbol{\tau} = \boldsymbol{\gamma} \cdot \mathbf{I}_{\mu} \quad \text{in } \mathscr{D} \,, \tag{16}$$

where $\boldsymbol{\sigma}$ is the Cauchy macrostress tensor, $\boldsymbol{\tau}$ is the relative (interactive) stress tensor and $\boldsymbol{\mu}$ is the double (micro)stress tensor, $\boldsymbol{\gamma}$ is the micro-acceleration, ρ is the density and $\mathbf{I}_{\mu}$ is the second moment of micro-density. The macrostress can be viewed in a classical manner as the macroscopic average of forces per unit area, while the microstress can be interpreted as a spatial average of the forces arising from the collective non-local behavior of the surrounding microstructure.

Concerning the stress and strain measures, we generalize the conventional concept by replacing the Cauchy stress tensor by a generalized stress tensor such that, in the Voigt notation (in which a 9 by 9 tensor can be replaced by a 27-dimensional vector), the generalized stress tensor is expressed as

$$\boldsymbol{\Sigma} = [\boldsymbol{\sigma} \,,\, \boldsymbol{\tau} \,,\, \boldsymbol{\mu}] \,. \tag{17}$$

Similarly a generalized strain tensor can be expressed as,

$$\mathbf{E} = [\boldsymbol{\varepsilon} \,,\, \boldsymbol{\varepsilon} - \boldsymbol{\chi} \,,\, \nabla \cdot \boldsymbol{\chi}] \,, \tag{18}$$

where $\boldsymbol{\varepsilon} = \nabla \cdot \mathbf{u}$ is the classical Cauchy strain tensor and $\boldsymbol{\chi}$ is the microstrain tensor such that the microdisplacement can be approximated by $u'_i = x'_j \chi_{ji}(x_i, t)$.

In the elastic regime the generalized stress and strain are linearly related through a generalized elastic stiffness tensor $\bar{\mathbb{C}}$ that can be written as a block diagonal matrix,

$$\bar{\mathbb{C}} = \begin{bmatrix} \mathbb{C}^0 & \mathbb{A}^{0\mu} & 0 \\ \mathbb{A}^{0\mu} & \mathbb{C}^{0\mu} & 0 \\ 0 & 0 & \mathbb{C}^{\mu} \end{bmatrix} \,, \tag{19}$$

where $\mathbb{C}^0$ is the macroscopic stiffness tensor, $\mathbb{C}^{\mu}$ is the microscopic stiffness tensor introducing a length scale parameter associated with the microstructure, $\mathbb{C}^{0\mu}$ is a transition stiffness tensor between the macroscopic and microscopic kinematics and $\mathbb{A}^{0\mu}$ another coupling term. In this work, we assume that there is no elastic coupling among the macro- and micro-scales ($\mathbb{A}^{0\mu} = 0$). The tensor $\mathbb{C}^{0\mu}$ is assumed to be associated with a softening/stiffening microstructure such that the resistance to local deformation in the microstructured solid is less/more than the resistance to macroscopic deformation, i.e. $\mathbb{C}^{0\mu} = \alpha_1 \mathbb{C}^0$. The microstructural stiffness tensor $\mathbb{C}^{\mu}$ contains information about the length scale $\bar{\ell}$ of heterogeneity in the microstructured solid and is taken for simplicity as the second moment of stiffness over the microvolume $\Omega(M)$, i.e. $\mathbb{C}^{\mu} = \bar{\ell}^2 \alpha_1 \mathbb{C}^0$. Overall, the elastic micro-continuum constitutive model is characterized by two additional constitutive parameters: α_1 and $\bar{\ell}$.

The constitutive relation in the plastic regime is based on a classical J2 plasticity model at the macroscopic level while the microscopic level is assumed to stay elastic. Again we point out that that the focus of this work is on developing multi-resolution schemes to study the dynamic

behavior of heterogeneous materials, rather than the physical models themselves. Therefore no specific effort has been dedicated in developing a microscale plasticity model. In this context, the plastic potential $\Phi(\boldsymbol{\sigma}, \kappa)$ is assumed to be solely a function of the Cauchy macrostress tensor and of the equivalent plastic strain κ such that,

$$\boldsymbol{\varepsilon}^p = \dot{\lambda} \frac{\partial \Phi}{\partial \boldsymbol{\sigma}} , \tag{20}$$

where $\boldsymbol{\varepsilon}^p$ is the plastic deformation, $\dot{\lambda}$ is a Lagrange plastic multiplier and $\partial\Phi/\partial\boldsymbol{\sigma}$ denotes the direction of the plastic flow. As in conventional plasticity, the stress point must remain on the yield surface during plastic deformation, which gives the consistency condition for continuing plastic flow :

$$\frac{\partial \Phi^{\mathrm{T}}}{\partial \boldsymbol{\sigma}} \dot{\boldsymbol{\sigma}} + \frac{\partial \Phi}{\partial \kappa} \dot{\kappa} = 0 . \tag{21}$$

If we use the gradient to the yield surface $\mathbf{n}$ according to

$$\mathbf{n} = \frac{\partial \Phi}{\partial \boldsymbol{\sigma}} , \tag{22}$$

and the hardening/softening modulus h as defined in conventional plasticity :

$$h = -\frac{1}{\dot{\lambda}} \frac{\partial \Phi}{\partial \kappa} \dot{\kappa} , \tag{23}$$

the consistency equation can be rewritten as,

$$\mathbf{n}^{\mathrm{T}} \dot{\boldsymbol{\sigma}} - h\dot{\lambda} = 0 . \tag{24}$$

In this paper, we apply the strain-hardening/softening hypothesis as defined by

$$\dot{\kappa} = \sqrt{\frac{2}{3} \boldsymbol{\varepsilon}^p : \boldsymbol{\varepsilon}^p} , \tag{25}$$

combined with the Von Mises yield criteria based on the second invariant of the stress tensor.

For the sake of comparison with more classical homogenization methods, the composite macroscale response is also computed by assuming a uniform normal stress in the direction of propagation given the mass fractions m_i and the constitutive behavior of the individual materials in a classical rule of mixture manner. When non-linear compressibility is accounted for, a Mie-Grüneisen equation of state is used. This method is referred to as homogenization in the rest of this manuscript.

Extracting microcontinuum constitutive relationships from DNS

Before analyzing the dynamic response of MMCs and heterogeneous materials through the present multi-resolution continuum model, we will briefly overview the last step of the construction of this model which consists of extracting the microcontinuum constitutive relationships from the DNS

calculations. The goal is achieved here by minimizing the error between the response given by DNS with the one obtained from the microcontinuum model. Note that many strategies can be adopted to optimize and calibrate the parameters from the microcontinuum model to give a best fit to the DNS results, but this discussion is beyond the scope of this article. In this work, in order to calibrate the microcontinuum parameters, we chose to minimize the error between the average velocity given by the DNS with the one obtained from the microcontinuum model. Calibration starts by defining a conventional 3D RVE and loading with a given compressive pulse input. The average of the velocity over the transverse plane (normal to the propagation direction) is recorded and used to calibrate the microcontinuum model. This is done through a classical multidimensional least square method such that, if the microcontinuum constitutive model is described by a set of n parameters $[\alpha_1, \cdots, \alpha_n]$, those can be extracted from the DNS simulations through,

$$[\alpha_1, \cdots, \alpha_n] = \underset{[\alpha_1, \cdots, \alpha_n]}{\arg\min} \left(\int_t \int_x \left(\int_y \int_z v^{dns}(x,y,z,t) - v^{\mu}(x,t;[\alpha_1, \cdots, \alpha_n]) \right)^2 dx\, dt \right) , \tag{26}$$

where $v^{dns}(x,y,z,t)$ is the velocity obtained from DNS, while $v^{\mu}(x,t;[\alpha_1, \cdots, \alpha_n])$ is the velocity from the microcontinuum calculation. In the case of our elastic microcontinuum model, calibration is done for the microstructural parameters, α_1 and $\bar{\ell}$.

As an illustration of the data extraction methodology, we use a specific example involving a linear elastic layered Al/SiC composite as shown by the schematic in Figure 4. Each layer of the composite has a thickness of $\ell = 250\mu$m and is assumed to behave elastically. DNS have been performed on this one-dimensional configuration and used as a basis for extracting the microcontinuum constitutive parameters which reduce to two parameters $\left(\alpha_1, \bar{\ell}\right)$ in the elastic regime based on equation (26). Figure 5(a) presents the results of the calibration of the microcontinuum model done for a compressive loading pulse of a given width and height. Based on this calibration, parameters for the microcontinuum model are given by $\bar{\ell} = 165\mu$m and $\alpha_1 = 0.0618$. Note that the microcontinuum length scale $\bar{\ell}$ is slightly different than the physical length scale ℓ associated with the thickness of the layers of the Al/SiC composite. $\bar{\ell}$ could be interpreted as a characteristic dispersion length. The parameter α_1 could be interpreted as a softening microstructure such that the resistance to local deformation in this microstructured layered composite is less than the resistance to macroscopic deformation. It is also worthwhile to note the qualitative agreement between DNS and the microcontinuum model. In contrast with the results from static homogenization, the microcontinuum model picks up the dispersive character of a loading wave propagating through the medium. In order to verify that these parameters are indeed a reflection of microstructural effects, the same microstructure was subjected to different loading inputs and results were computed keeping the calibrated parameters fixed. Figure 5(b) and Figure 5(c) show the effect of halving and doubling respectively the input pulse width while keeping an excellent quantitative comparison with the DNS. Figure 5(d) illustrates the same comparison for a symmetric impact loading configuration. Again, the agreement between the DNS and the microcontinuum model is preserved. In other words, only a limited number of RVEs and DNS are required to calibrate the constitutive relationships of the aforementioned microcontinuum model. It is also worth pointing out that certain qualitative features given by the DNS results are absent from the classical homogenization such as the attenuation of the peak velocity or the higher frequency ringing after the initial pulse.

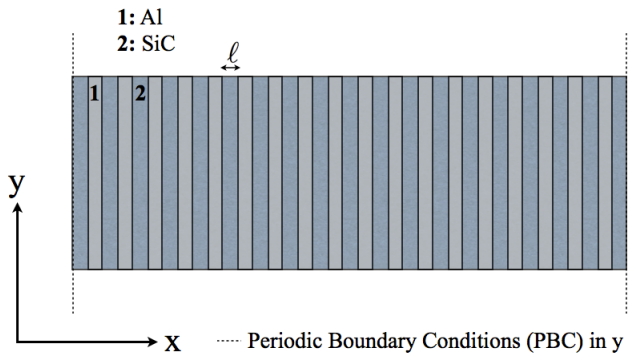

Figure 4. Schematic of a layered medium used for calibration.

2.3 Results and Discussion

The DNS model presented in section 2.1 and the microcontinuum model overviewed in the previous section 2.2 are first applied to a layered and then to a prototypical particulate-reinforced Al/SiC MMC. The layered composite can be viewed as a one dimensional (1D) heterogeneous medium while the particulate-reinforced composite is considered as a fully 3D microstructured medium.

First, we consider the comparison between the results obtained from the microcontinuum model of a nonlinear elastoplastic 1D layered composite with those obtained by DNS. Following the procedure presented in section 2.2, Figure 6 presents the comparisons between DNS and the microcontinuum model in the elastoplastic regime. Similar to the purely elastic case, a good agreement is found between DNS and the reduced model. Specifically the pulse widening and attenuation that is observed in the DNS in the case of a short pulse (see Figure 6(b)) is captured by the microcontinuum model. This observation is due to the fact that the length scale associated with the input pulse is of the same order of magnitude as the microstructural features of the 1D composite. In contrast, Figure 6(c) shows the response to a substantially wider input pulse. In this case, the dispersion of the wave propagating through the microstructured medium is not as pronounced. More interestingly, in the case of an impact loading (see Figure 6(d)), both the DNS and microcontinuum model exhibit the continuous broadening of the wave front as it propagates, as opposed to the classical homogenization method which show two sharp elastic fronts. The results given by the microcontinuum model of wave propagating through the layered composite are consistent with those calculated through DNS but without the associated computational cost. Note that the above features evident in the microcontinuum model and DNS simulations are not captured by the homogenization method because dispersive effects are not present in classical homogenization models.

Second, we examine the case of a three dimensional particulate-reinforced Al/SiC MMC (see section 2.1) subjected to a short duration pulse input. Recall that, even though at the continuum scale this is generally considered a uniaxial strain condition, at the scale of the microstructure the deformation state is fully three dimensional. Ideally, one would have models that capture the

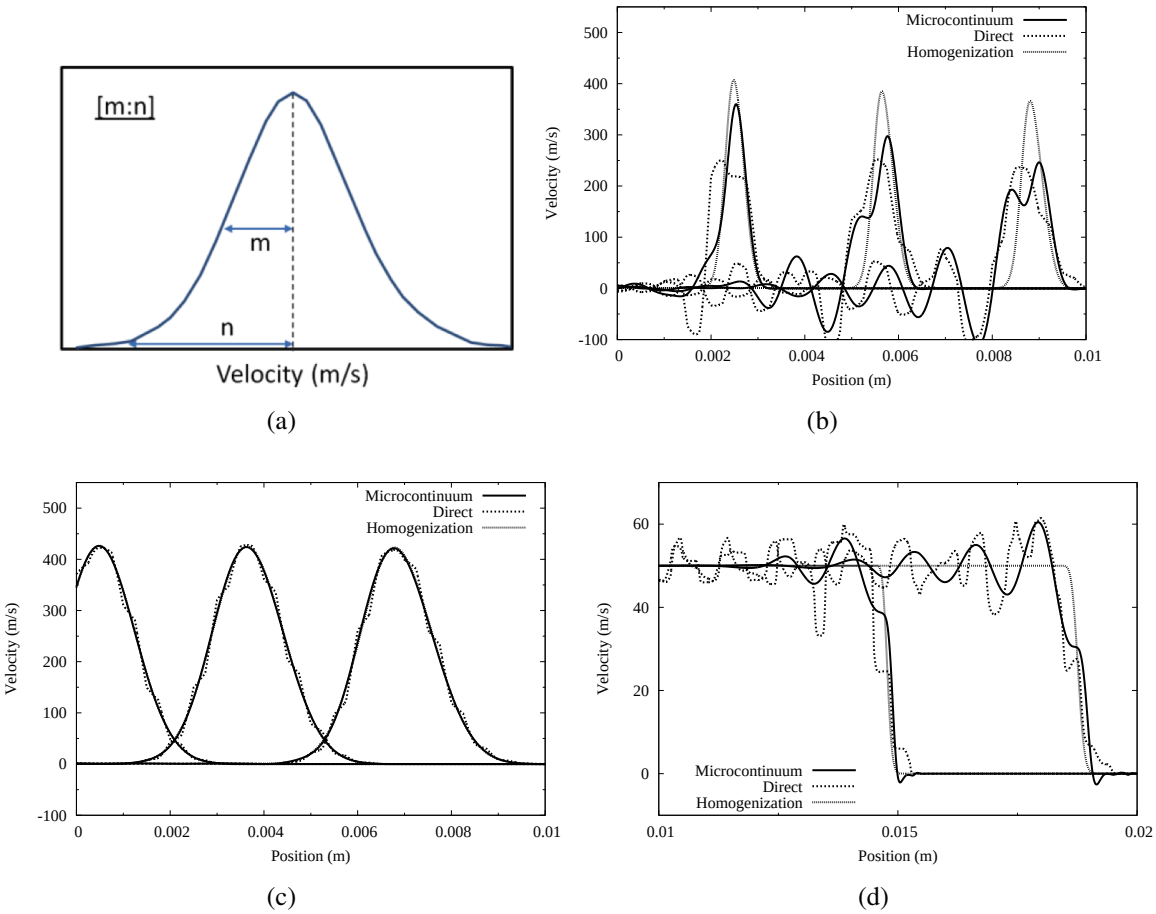

Figure 5. Comparison of predicted velocity profiles between DNS and the microcontinuum model for a 1D layered Al/SiC composite in the elastic regime. (a) For a Gaussian input used for initial calibration (b) for a short pulse loading (c) for a long pulse loading (d) for an impact loading.

dispersion effects associated with the three dimensionality of the micro-scale response. Figure 7 illustrates how the present multi-resolution scheme constitutes a step in this direction. The DNS incorporates the dispersion behavior of the microstructure directly, so the rate at which the compressive wave steepens due non-linear stiffening of the volumetric response will be reduced [42]. In the case of the one dimensional models, the classical homogenization method tends to steepen more rapidly as the wave propagates due to its non-dispersive nature; however, the microcontinuum model encapsulates some of the features from the DNS and strikes a balance between the nonlinear volumetric response and dispersion due to the microstructural character of the medium.

The overall trend of the influence of microstructural bias emerging from this multi-resolution paradigm illustrates the predictive capability of the microcontinuum model compared to fully resolved models and shows its applicability in the study of dynamic response of heterogeneous mate-

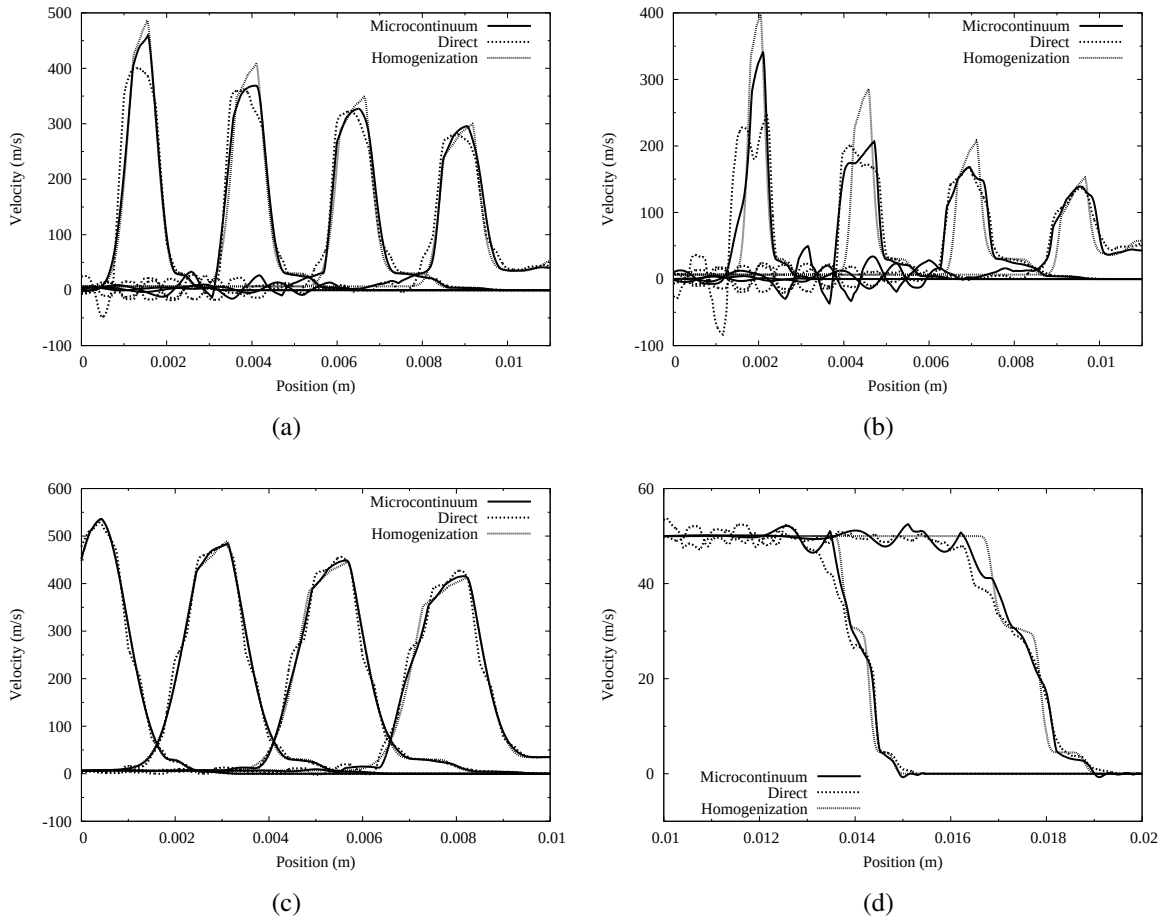

Figure 6. Comparison of predicted velocity profiles between DNS and the microcontinuum model for a 1D layered Al/SiC composite in the elasto-plastic regime. (a) For a Gaussian input pulse (b) for a short pulse loading (c) for a long pulse loading (d) for an impact loading.

rials. Although this approach has shown promise, there are outstanding issues that warrant further attention:

- In this work the microscale response was strictly elastic while the comparison with DNS might benefit from an elasto-plastic model at this scale. In a separate work [23], we have examined the impact of microscale plasticity on dispersive behavior, and it is currently under investigation.

- The DNS data that was used in the extraction was an average over the transverse plane. An improvement would be to develop data extraction techniques that incorporate lateral spatial variation present in the three dimensional DNS into the resulting microstructural parameters, thereby accommodating more information from the DNS.

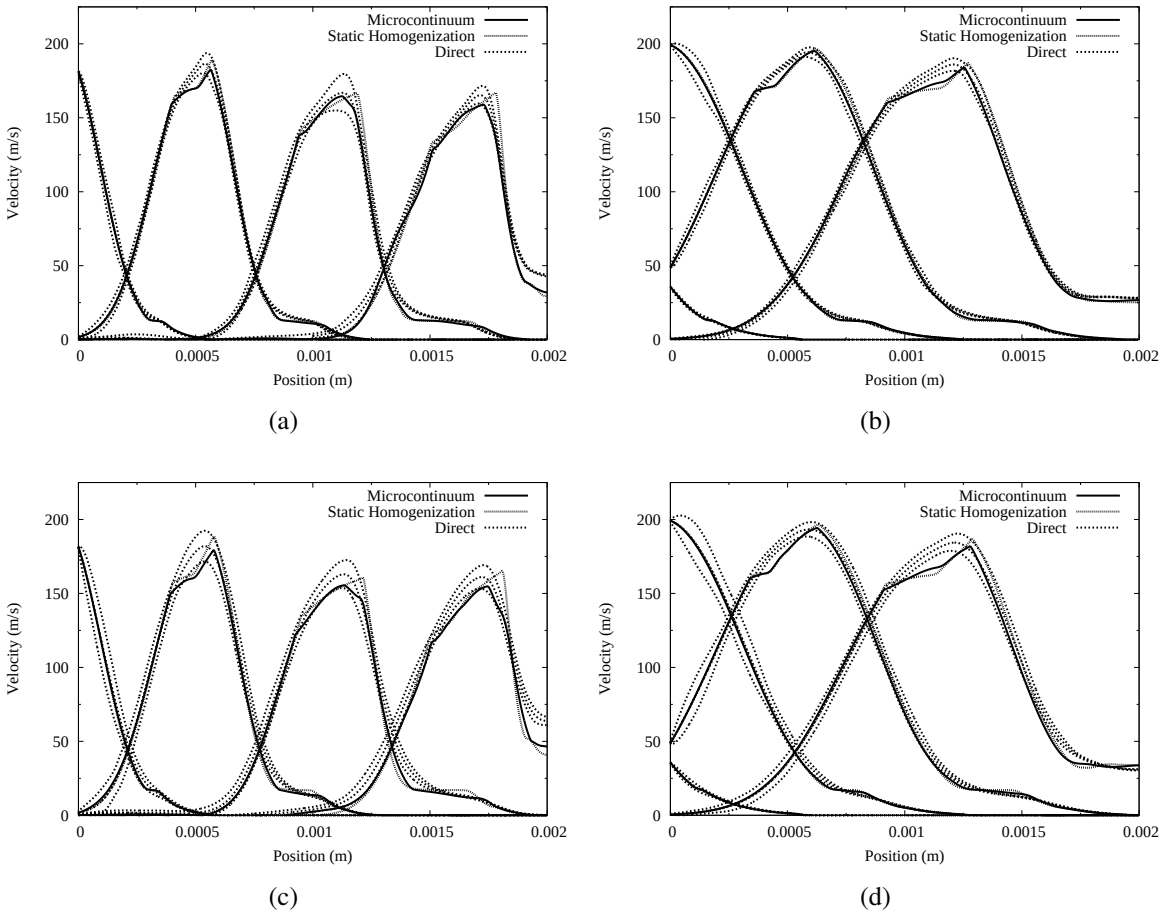

Figure 7. Comparison of predicted velocity profiles between DNS and the microcontinuum model for a 3D particulate-reinforced Al/SiC MMC in the elastoplastic regime. The profiles shown of the DNS results are the average of three random microstructural realizations and include an upper and lower envelop that shows the standard deviation in velocity on the transverse plane at the given position. (a) For a Gaussian input pulse with a volume fraction of SiC of 5% (b) for a long pulse loading with a volume fraction of SiC of 5% (c) for a Gaussian input pulse with a volume fraction of SiC of 10% (b) for a long pulse loading with a volume fraction of SiC of 10%

- While our goal is to develop a lower dimensional model for planar wave propagation, the transition from 3D DNS to 1D microcontinuum may incur too much information loss for some applications. Future work will use similar data extraction techniques to inform 3D microcontinuum models which will be used to quantify the information loss through different levels of abstraction.

- Another issue of considerable interest to the dynamic materials community is the dependence

of shock formation rate and eventual thickness on material microstructure. Our results indicate these dispersion effects can be represented by the microcontinuum formulation and can be improved by refining the physical models both for the DNS and the microcontinuum model.

- In order for the numerical methods in this work to be used with confidence, experimental validation is required. We are currently developing plate impact experiments in well characterized polycrystalline copper using photon doppler velocimetry for this purpose. Further experiments in MMCs are warranted.

2.4 Conclusions of Multi-Resolution Analysis

A multi-resolution continuum paradigm has been presented to study the dynamic behavior of heterogeneous materials such as MMCs. This framework relies on DNS to spatially resolve the complexity and richness of a wave propagating through microstructured heterogeneous media. The DNS model is based on a combination of a crystal plasticity formulation for the non-linear behavior of the host matrix and the Johnson–Holmquist (JH-1) model for behavior of the particulate reinforcements. Results from the mesoscale DNS inform a non-linear plastic microcontinuum model which introduces richer kinematics to account for microstructural features without explicitly modeling them and with far fewer total degrees of freedom. The microcontinuum model is based on the mechanics of generalized continua and introduces characteristic parameters (characteristic microstructural length scale and microstructural materials parameters for example) arising from the inhomogeneous behavior of the microstructure. These parameters are generally related to microstructural features such as grains and particulate reinforcements.

The resulting multi-resolution continuum framework can predict the evolution of continuum fields propagating through a microstructured medium without having to perform the fully resolved microstructural simulations for each loading configuration. Only the DNS used for the calibration of these models are required to determine the microstructural parameters used in the definition of the constitutive behavior of the microcontinuum model.

This multi-resolution paradigm has been applied to model the dynamic behavior of layered and particulate reinforced Al/SiC MMCs. The results from the calibrated microcontinuum model are consistent with those calculated through DNS but without the associated computational cost. Qualitative comparisons of this multi-resolution scheme with classical homogenization methods suggest that the result obtained are be more realistic for a wide range of compressive loading inputs. In particular, the dispersive characteristics seem to be better captured when microscale features are in the same order of magnitude as the microstructure. Again, we note that the classical homogonization technique we compare to *cannot* capture these dispersive effects as those physics are *not* present in that model.

Such results show great promise for developing accurate and efficient modeling tools and establish the connection between microstructure and properties. As such, this type of paradigm would be useful in developing new materials with optimal properties for high strain rate conditions. For

the same reason, such a paradigm would enable and improve our understanding of deformation mechanisms in heterogeneous materials at high strain rates.

3 Dispersion due to microstructural features

The dynamic thermomechanical response of materials (e.g. metals, ceramics, foams, or composites) is profoundly influenced by an underlying microstructure consisting of heterogeneities of various shape and spatial arrangements, precipitates, and defects clusters (collections of dislocations, distribution of cracks and/or porosity for example). The effects of these heterogeneities on the dynamic response are particularly pronounced when the scale of the deformation is of the order of the material microstructural heterogeneities or when its order of magnitude is comparable to the short wavelength of a signal propagating through the material. For example, it has been experimentally observed that the dynamic strength of polycrystalline metals is impacted by heterogeneities, such as microvoids for instance, leading to localization of deformation and loss of shear strength [82, 120]. Wave scattering due to the mismatch in mechanical impedance at the interface between different material phases in layered composites [125] is another illustration of the impact of microstructural features on the dynamic response of materials. The dispersive nature of wave propagation in microstructured materials plays an important role in localization phenomena in dynamic problems. In conventional continuum formulations, the governing partial differential equations may lose hyperbolicity at a certain stage of a nonlinear deformation process. This means that loading waves can no longer propagate and the deformation is trapped in an infinitely narrow band in which the strain can grow unboundedly [96, 9, 93].

Despite the conspicuous experimental observations of the dispersive character of microstructured materials [77, 105, 88, 87, 11, 68, 104, 55, 114, 36] for a wide variety of materials, the classical continuum mechanics theory predicts that frequency and wave number have a linear relationship (i.e. phase and group velocities of propagating waves are independent of the frequency) and therefore fails to successfully model the impact of microstructural features and their associated length scales on wave dispersion. Propagation of elastic waves in a one-dimensional (1D) domain is analyzed with the well-known d'Alembert or Riemann solutions (see for example [1]). Extension to nonlinear wave propagation has been studied extensively in the context of classical continuum mechanics, see [65, 59, 50, 51, 81]. The review article by [91] provides a comprehensive review of nonlinear wave propagation in solids. However, microstructural features are not represented and considered in these formulations.

Numerous advanced theories and models have been proposed to study wave propagation problems accounting for heterogeneities and non-locality in materials. Among them, multiscale homogenization techniques [62, 17, 3] have proved to be successful in capturing dispersion effects. The idea in this type of approach is to asymptotically compute the solutions to the wave equations using multiple spatial and temporal scales to capture the homogenized solution as well as its long-term behavior. Alternatively, models based on the mechanics of generalized continua constitute another class of paradigms used to incorporate some effects of characteristic lengths of the materials microstructure. The idea here is to endow the continuum with additional degrees of freedom that are supposedly independent from the usual translational degrees of freedom and representative of the microstructure [34]. The article by [39] and the book by [30] provide a detailed review of the mechanics of higher order continua. Analytical studies of the dispersive character of such high order continua have been initially conducted in depth by [84], [31] or more recently by [26, 28] or

[92] for linear elastic solids.

In this section, we study the wave propagation and wave dispersion character in hardening elasto-plastic microstructured materials on the basis of generalized continua theories. The adopted model accounts for the microstructural features complemented by a hardening elasto-plastic model through a deformation theory of plasticity. We limit our considerations to the case where plastic strains are large compared to the elastic strain. Nonlinearity is introduced in this study only through the description of the yield surfaces during plastic deformation both at the macroscopic and microscopic level.

The following notation is used:

$\mathbf{u}, \mathbf{u}'$: macro- microscopic displacement field.

v: macroscopic velocity.

ε, χ: macro- microdeformation.

$\varepsilon^{el}, \chi^{el}$: elastic macro- microstrain.

$\varepsilon^{p}, \chi^{p}$: plastic macro- microstrain.

σ, μ: macro- microstress.

η: $-$interactive microforce.

$\mathscr{W}, \mathscr{K}, \mathscr{L}$: potential energy, kinetic energy and Lagrangian.

ρ, I_μ: macroscopic density and micro-inertia.

E_0: $-$Young's modulus.

$A_{0\mu}, B_{0\mu}, E_\mu$: microstructure elastic parameters.

h_0, h_μ: macro- microscopic hardening/softening moduli.

$\rho_\mu, \beta_{0\mu}$: dimensionless parameters.

c_i: macroscopic/microscopic characteristic velocity "i".

γ_i: normalized characteristic velocity "i" corresponding to velocity c_i.

$\ell, \bar{\ell}, \mathscr{L}_0, \lambda_0$: characteristic lengths.

τ: characteristic time.

ε_ℓ,: scale of the microstructure.

ϖ, κ, λ: dimensionless frequency, wave number and wave length.

γ_π: dimensionless phase velocity.

γ_g: dimensionless group velocity.

$\bar{c}$, c_s: non normalized/normalized gradient-dependent parameters.

$[\cdot]_x, [\cdot]_t$: subscript in x and t denote differentiation with respect to these indices.

$\tilde{[\cdot]}$: tilde superscript indicates non-dimensional variables and operators.

$[\cdot]'$: denotes the derivative with respect to a given variable.

3.1 Formulation of a nonlinear 1D micromorphic model

One-dimensional wave equation for nonlinear microstructured materials

Following [84], let us consider a continuum as a deformable continuous distribution of material points, each of them being geometrically represented by a point M and characterized kinematically by macroscopic and microscopic displacement fields. The macroscopic displacement field $\mathbf{u}$ is defined as $u_i = x_i - X_i, i = 1 \ldots 3$, where x_i and X_i are the coordinates of a materials in the deformed and undeformed reference coordinate system respectively. The microdisplacement $\mathbf{u}'$ is defined by its components $u'_i = x'_i - X'_i$, where x'_i are the coordinates of a point M' belonging to a microvolume $\Omega(M)$ around M and measured from the center of mass M of this microvolume. Given $\Omega(M)$ of small extent and displacement gradients assumed to be small, the microdisplacement can be approximated by

$$u'_i = x'_j \chi_{ji}(x_i, t) \ , \tag{27}$$

where χ_{ji} is the microdeformation defined by,

$$\chi_{ji} = \frac{\partial u'_j}{\partial x'_i} \ . \tag{28}$$

In the 1D case, the indices can be dropped. In the remainder of this manuscript, subscript indices in x and t denote differentiation with respect to these indices. For example, $[\cdot]_x = \partial/\partial x$ and $[\cdot]_{tt} = \partial^2/\partial t^2$.

Following a similar approach to [26], the fundamental balance laws for a microstructured material are derived from the system Lagrangian $\mathscr{L}$ such that,

$$\mathscr{L} = \mathscr{K} - \mathscr{W} \ , \tag{29}$$

where the kinetic energy $\mathscr{K}$ is defined as,

$$\mathscr{K} = \frac{1}{2}\rho {u_t}^2 + \frac{1}{2} I_\mu {\chi_t}^2 \ , \tag{30}$$

with ρ and I_μ being the macroscopic density and micro-inertia respectively and the potential energy $\mathscr{W}$ is defined as,

$$\mathscr{W} = \mathscr{W}(u_x, \chi, \chi_x) \ . \tag{31}$$

The corresponding Euler-Lagrange equations take the form,

$$\left(\frac{\partial \mathscr{L}}{\partial u_t}\right)_t + \left(\frac{\partial \mathscr{L}}{\partial u_x}\right)_x - \frac{\partial \mathscr{L}}{\partial u} = 0 \,, \tag{32a}$$

$$\left(\frac{\partial \mathscr{L}}{\partial \chi_t}\right)_t + \left(\frac{\partial \mathscr{L}}{\partial \chi_x}\right)_x - \frac{\partial \mathscr{L}}{\partial \chi} = 0 \,. \tag{32b}$$

The resulting equations of motion are therefore,

$$\rho u_{tt} - \left(\frac{\partial \mathscr{W}}{\partial u_x}\right)_x = 0 \,, \tag{33a}$$

$$I_\mu \chi_{tt} - \left(\frac{\partial \mathscr{W}}{\partial \chi_x}\right)_x + \frac{\partial \mathscr{W}}{\partial \chi} = 0 \,. \tag{33b}$$

Alternatively, the balance equations for a microstructured material in 1D can be expressed by,

$$\rho u_{tt} - \sigma_x = 0 \,, \tag{34a}$$

$$I_\mu \chi_{tt} - \mu_x + \eta = 0 \,, \tag{34b}$$

with,

$$\sigma = \frac{\partial \mathscr{W}}{\partial u_x} \,,\ \mu = \frac{\partial \mathscr{W}}{\partial \chi_x} \,,\ \text{and}\ \eta = \frac{\partial \mathscr{W}}{\partial \chi} \,. \tag{35}$$

σ is the macrostress (Piola stress), μ the microstress and η is the interactive microforce. The macrostress can be viewed in a classical manner as the macroscopic average of forces per unit area, while the microstress can be interpreted as a spatial average of the forces arising from the collective nonlocal behavior of the surrounding microstructure. Note that in the above equations, no apparent explicit coupling occurs between the thermodynamic quantities associated with macro- and microdeformations. The effective coupling between the two is accounted for in the potential energy functional. The first of equation (34) describes the macroscopic balance of momentum while the second of equation (34) expresses the microscopic balance of momentum. In the case of elasticity, it is convenient to consider a generic potential energy function describing the constitutive behavior of microstructured materials as followed,

$$\mathscr{W}\left(u_x, \chi, \chi_x\right) = \frac{1}{2}\left(E_0 + 2A_{0\mu} + B_{0\mu}\right) u_x^2 + \frac{1}{2} E_\mu \chi_x^2 + \frac{1}{2} B_{0\mu} \chi^2 - \left(A_{0\mu} + B_{0\mu}\right) \chi u_x \,, \tag{36}$$

where E_0 is the Young's modulus, and $\left(A_{0\mu}, B_{0\mu}, E_\mu\right)$ are microstructure elastic parameters. Obviously, the choice of such a potential energy function assumes that a certain correlation exists between the parameters describing the macroscopic behavior and the microscopic behavior. The coefficients for this generic potential energy function have been chosen is such a way that they are consistent with both the formulation of [26] and that of [40] and coworkers. Details on the nonlinear term will be discussed hereafter. Note that the coupling between the macro and microdeformation is accounted for through the coefficient $A_{0\mu} + B_{0\mu}$. Another solution for the coupling between the macro and microdeformation could have been of the form $\left(A'_{0\mu} + B_{0\mu}\right) \chi_x u_x$, or a linear combination of the two.

The linear elastic Hooke's law is usually inadequate to describe materials nonlinear, inelastic behavior. In this work, we therefore consider a plasticity formulation that incorporates a dependence upon the inelastic strain and a coupling between the macro- and microdeformation. As such, in the context of small strain conditions, the total macro- and microdeformation are partitioned into a thermoelastic (elastic and thermal dilatation) $\left(\varepsilon^{el}, \chi_x^{el}\right)$, and an inelastic $\left(\varepsilon^{p}, \chi_x^{p}\right)$ macro- microstrain respectively such that,

$$\varepsilon^p = \varepsilon - \varepsilon^{el} = u_x - \frac{\sigma}{E_0 + 2A_{0\mu} + B_{0\mu}} - \frac{A_{0\mu} + B_{0\mu}}{E_0 + 2A_{0\mu} + B_{0\mu}} \chi^{el} \ , \tag{37a}$$

$$\chi_x^p = \chi_x - \chi_x^{el} = \chi_x - \frac{\mu}{E_\mu} \ , \tag{37b}$$

where the infinitesimal macrostrain is classically defined as $\varepsilon = u_x$ and the elastic component of the macrostrain and microstrain is related to the macro- and microstress via the bijective relation

$$\sigma = \frac{\partial \mathscr{W}}{\partial u_x} = \left(E_0 + 2A_{0\mu} + B_{0\mu}\right) \varepsilon^{el} - \left(A_{0\mu} + B_{0\mu}\right) \chi^{el} \ , \tag{38a}$$

$$\mu = \frac{\partial \mathscr{W}}{\partial \chi_x} = E_\mu \chi_x^{el} \ . \tag{38b}$$

Concerning the macro- and microyield functions, at the macroscopic level, we consider a classical J_2 plasticity model in which the yield strength depends upon the equivalent plastic strain (in the sense of the von Mises strain invariant). At the microscopic level, we consider that the microstrength only depends upon the equivalent plastic microstrain strain. The interactive force is assumed to remain an elastic coupling between the two length scales. As such, we assume that the constitutive equations (35) in the plastic regime can be written in rate form such that $\sigma_t = f\left(\varepsilon_t^p\right)$ and $\mu_t = g\left([\chi_x^p]_t\right)$ yielding,

$$\sigma_t = \frac{1}{h_0 - 1} E_0 \varepsilon_t^p \ , \tag{39a}$$

$$\mu_t = \frac{1}{h_\mu - 1} E_\mu \left(\chi_x^p\right)_t \ , \tag{39b}$$

$$\eta_t = -\left(A_{0\mu} + B_{0\mu}\right) \varepsilon_t^{el} + B_{0\mu} \chi_t^{el} \ . \tag{39c}$$

where $\left(h_0, h_\mu\right)$ are the hardening/softening macro-modulus and micro-modulus respectively. Due to physical considerations (tangent plastic modulus), $\left(h_0, h_\mu\right) \notin (-1, 1)$. Note that the continuum becomes elastic when $h_0 = 1$ and $h_\mu = 1$ and becomes perfectly plastic when $h_0 \to \infty$ and $h_\mu \to \infty$. Macro- or micro- hardening occurs when $h_0 > 1$ or $h_\mu > 1$ respectively. Macro- or micro- softening occurs when $h_0 < -1$ or $h_\mu < -1$ respectively.

Combining equations (34), (37) and (39), and defining the velocity $v = u_t$ the system of second order equations (34) can be represented in the form of one fourth-order nonlinear equation. The resulting wave equation for a one-dimensional hardening microstructured medium is given by,

$$\frac{1}{\bar{c}^2} \frac{c_{0\mu}^2}{\bar{c}^2} v_{tt} = \left(1 - \frac{c_{0\mu}^2}{\bar{c}^2}\right) \left[v_{xx} - \frac{\bar{h}}{\bar{c}^2} v_{tt}\right] + \tau^2 h_\mu \left[v_{xx} - \frac{\bar{h}}{\bar{c}^2} v_{tt}\right]_{tt} - c_\mu^2 \tau^2 \left[v_{xx} - \frac{\bar{h}}{\bar{c}^2} v_{tt}\right]_{xx} \ , \tag{40}$$

where the characteristic velocities are defined as,

$$c_0^2 = \frac{E_0}{\rho} \ , \ \bar{c}^2 = \frac{E_0 + 2A_{0\mu} + B_{0\mu}}{\rho} \ , \ c_{0\mu}^2 = \frac{\left(A_{0\mu} + B_{0\mu}\right)^2}{\rho B_{0\mu}} \ , \ c_\mu^2 = \frac{E_\mu}{I_\mu} \ , \tag{41}$$

the characteristic microstructural time τ is given by,

$$\tau^2 = \frac{I_\mu}{B_{0\mu}} \ , \tag{42}$$

and the effective hardening modulus $\bar{h}$ is given by,

$$\bar{h} = h_0 + (h_0 - 1)\frac{\bar{c}^2 - c_0^2}{c_0^2} \ . \tag{43}$$

Details of the derivation of equation (40) are provided in the appendix A. Note that we recover the results from [26, 28] in the case of a linear elastic microcontinuum.

Equation (40) clearly emphasizes the hierarchy and dispersive character of waves propagating into the material. The coupling between the microstructure and macroscopic scale is reflected in the correction of the bulk phase velocity c_0 as illustrated on the left-hand side of (40). The right-hand terms of (40) are dominated by both the properties of the microstructure (micro-inertia) and the materials nonlinearity.

In the following, the microstructural parameter $B_{0\mu}$ is assumed to be associated with a softening/stiffening microstructure such that the resistance to local deformation in the microstructured solid is less/more than the resistance to macroscopic deformation. As such,

$$B_{0\mu} = \beta_{0\mu}^2 E_0 \ , \tag{44}$$

where $\beta_{0\mu}$ is the softening/stiffening coefficient. Similarly, for simplicity, the coupling between the macro- and microdeformation $A_{0\mu}$ is assumed to be correlated to the macroscopic resistance and microscopic resistance such that,

$$A_{0\mu} = \left(\gamma_{0\mu} - \beta_{0\mu}\right)\beta_{0\mu} E_0 \ . \tag{45}$$

Note that depending on the value of $\beta_{0\mu}$ and $\gamma_{0\mu}$, $A_{0\mu}$ could very well be a negative quantity (i.e when $\beta_{0\mu} > \gamma_{0\mu}$).

The micro-inertia I_μ introduces into the model one characteristic length scale parameter ℓ associated with the microstructure. It is taken as the second moment of stiffness over a given micro-volume $\Omega(M)$ weighted by a scaling factor ρ_μ such that,

$$I_\mu = \rho_\mu \rho \ell^2 \ . \tag{46}$$

For example in the case of a microstructured material containing microvoids, ρ_μ would be less than one, and in the case of a microstructured material containing dense micro-inclusions, ρ_μ would be greater than one. Note that due to physical considerations $\rho_\mu \geq 0$.

The microstructural parameter E_μ contains information about the scale of heterogeneity in the microstructured solids considered. Again for simplicity, E_μ is assumed to be proportional to the product of the macroscopic elastic constants and the square of the characteristic length scale such that,

$$E_\mu = \gamma_\mu^2 E_0 \ell^2 \ . \tag{47}$$

As such, the characteristic velocities and time parameters introduced in (41) and (42) reduce to

$$\bar{c}^2 = \left(1 + 2\gamma_{0\mu}\beta_{0\mu} - \beta_{0\mu}^2\right) c_0^2 = \bar{\gamma}^2 c_0^2 \ , \ c_{0\mu}^2 = \gamma_{0\mu}^2 c_0^2 \ , \ c_\mu^2 = \frac{\gamma_\mu^2}{\rho_\mu} c_0^2 \ , \ \tau^2 = \frac{\rho_\mu}{\beta_{0\mu}^2} \frac{\ell^2}{c_0^2} = \frac{\bar{\ell}^2}{c_0^2} \ . \tag{48}$$

Due to physical considerations, the term $\bar{\gamma}$ needs to stay positive or null, leading to restricted combinations of $\gamma_{0\mu}$ and $\beta_{0\mu}$ in the $\left(\gamma_{0\mu} - \beta_{0\mu}\right)$ input space as illustrated in Figure 8. This condition is a necessary but not sufficient condition for the mechanical wave to be physically acceptable. Note also that the characteristic length $\bar{\ell}$ is weighted by the effective rigidity of the microstructure $\dfrac{\rho_\mu}{\beta_{0\mu}^2}$.

The effective hardening modulus introduced in (43) reduces to,

$$\bar{h} = h_0 + \beta_{0\mu}\left(h_0 - 1\right)\left(2\gamma_{0\mu} - \beta_{0\mu}\right) = h_0 + \left(h_0 - 1\right)\left(\bar{\gamma}^2 - 1\right) \ . \tag{49}$$

Through non-dimensionalization, the wave equation (40) for a 1D hardening microstructured medium becomes

$$\frac{1}{\bar{\gamma}^2}\frac{\gamma_{0\mu}^2}{\bar{\gamma}^2} v_{\tilde{t}\tilde{t}} = \left(1 - \frac{\gamma_{0\mu}^2}{\bar{\gamma}^2}\right)\left[v_{\tilde{x}\tilde{x}} - \frac{\bar{h}}{\bar{\gamma}^2} v_{\tilde{t}\tilde{t}}\right] - \frac{1}{\varepsilon_\ell^2} h_\mu \left[v_{\tilde{x}\tilde{x}} - \frac{\bar{h}}{\bar{\gamma}^2} v_{\tilde{t}\tilde{t}}\right]_{\tilde{t}\tilde{t}} + \frac{1}{\varepsilon_\ell^2}\frac{\gamma_\mu^2}{\rho_\mu}\left[v_{\tilde{x}\tilde{x}} - \frac{\bar{h}}{\bar{\gamma}^2} v_{\tilde{t}\tilde{t}}\right]_{\tilde{x}\tilde{x}} \ , \tag{50}$$

where $x = \tilde{x}\mathscr{L}_0$, $t = \tilde{t}\mathscr{L}_0/c_0$, and $\varepsilon_\ell = \mathscr{L}_0/\bar{\ell}$ such that when ε_ℓ is small, microstructural effects can be neglected. $\mathscr{L}_0$ corresponds to the characteristic length of the wave propagating through the microstructured medium and $\mathscr{L}_0/c_0$ its corresponding characteristic time. We use a superimposed tilde to denote non-dimensional variables and operators.

Wave equation hyperbolicity

At this point it is interesting to discuss when the wave equation (50) will be physically acceptable and how the transfer of information occurs during propagation. In other words this subsection discusses when the wave equation remains hyperbolic and the initial value problem is well-posed. Equation (50) can be analyzed through its characteristics. If we consider the variation of the four third-order derivative terms of the velocity v, we get,

$$d\left(v_{\tilde{x}\tilde{x}\tilde{x}}\right) = v_{\tilde{x}\tilde{x}\tilde{x}\tilde{x}} d\tilde{x} + v_{\tilde{x}\tilde{x}\tilde{x}\tilde{t}} d\tilde{t} \ , \tag{51a}$$

$$d\left(v_{\tilde{x}\tilde{x}\tilde{t}}\right) = v_{\tilde{x}\tilde{x}\tilde{x}\tilde{t}} d\tilde{x} + v_{\tilde{x}\tilde{x}\tilde{t}\tilde{t}} d\tilde{t} \ , \tag{51b}$$

$$d\left(v_{\tilde{x}\tilde{t}\tilde{t}}\right) = v_{\tilde{x}\tilde{x}\tilde{t}\tilde{t}} d\tilde{x} + v_{\tilde{x}\tilde{t}\tilde{t}\tilde{t}} d\tilde{t} \ , \tag{51c}$$

$$d\left(v_{\tilde{t}\tilde{t}\tilde{t}}\right) = v_{\tilde{x}\tilde{t}\tilde{t}\tilde{t}} d\tilde{x} + v_{\tilde{t}\tilde{t}\tilde{t}\tilde{t}} d\tilde{t} \ . \tag{51d}$$

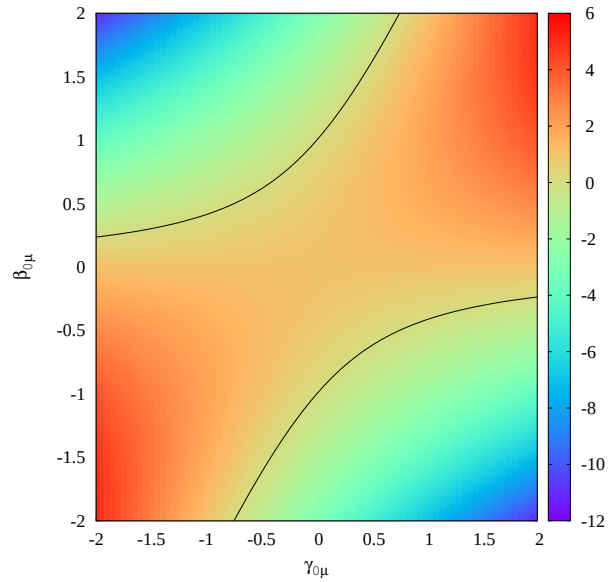

Figure 8. $\bar{\gamma}$ is defined in the $\left(\gamma_{0\mu} - \beta_{0\mu}\right)$ space between the solid lines.

Combining these equations with the 1D wave propagation equation, we obtain a system of five fourth order differential equations such that,

$$\begin{bmatrix} \frac{h_\mu \bar{h}}{\bar{\gamma}^2} & 0 & -\left[h_\mu + \frac{\gamma_\mu^2}{\rho_\mu}\frac{\bar{h}}{\bar{\gamma}^2}\right] & 0 & \frac{\gamma_\mu^2}{\rho_\mu} \\ 0 & 0 & 0 & d\tilde{t} & d\tilde{x} \\ 0 & 0 & d\tilde{t} & d\tilde{x} & 0 \\ 0 & d\tilde{t} & d\tilde{x} & 0 & 0 \\ d\tilde{t} & d\tilde{x} & 0 & 0 & 0 \end{bmatrix} \begin{bmatrix} v_{\tilde{t}\tilde{t}\tilde{t}\tilde{t}} \\ v_{\tilde{t}\tilde{t}\tilde{t}\tilde{x}} \\ v_{\tilde{t}\tilde{t}\tilde{x}\tilde{x}} \\ v_{\tilde{t}\tilde{x}\tilde{x}\tilde{x}} \\ v_{\tilde{x}\tilde{x}\tilde{x}\tilde{x}} \end{bmatrix} = \begin{bmatrix} f\left(v_{\tilde{t}\tilde{t}}, v_{\tilde{x}\tilde{x}}\right) \\ d\left(v_{\tilde{x}\tilde{x}\tilde{x}}\right) \\ d\left(v_{\tilde{x}\tilde{x}\tilde{t}}\right) \\ d\left(v_{\tilde{x}\tilde{t}\tilde{t}}\right) \\ d\left(v_{\tilde{t}\tilde{t}\tilde{t}}\right) \end{bmatrix}, \tag{52}$$

where the function $f\left(v_{\tilde{t}\tilde{t}}, v_{\tilde{x}\tilde{x}}\right)$ is defined by,

$$f\left(v_{\tilde{t}\tilde{t}}, v_{\tilde{x}\tilde{x}}\right) = \varepsilon_\ell^2 \frac{1}{\bar{\gamma}^2}\frac{\gamma_{0\mu}^2}{\bar{\gamma}^2} v_{\tilde{t}\tilde{t}} - \varepsilon_\ell^2 \left(1 - \frac{\gamma_{0\mu}^2}{\bar{\gamma}^2}\right)\left[v_{\tilde{x}\tilde{x}} - \frac{\bar{h}}{\bar{\gamma}^2} v_{\tilde{t}\tilde{t}}\right]. \tag{53}$$

Setting the determinant of the coefficient of the matrix of equation (52) yields the characteristic equation,

$$\bar{h} h_\mu d\tilde{x}^4 - \left[h_\mu \bar{\gamma}^2 + \bar{h}\frac{\gamma_\mu^2}{\rho_\mu}\right] d\tilde{x}^2 d\tilde{t}^2 + \bar{\gamma}^2 \frac{\gamma_\mu^2}{\rho_\mu} d\tilde{t}^4 = \left(\frac{\gamma_\mu^2}{\rho_\mu} d\tilde{t}^2 - h_\mu d\tilde{x}^2\right)\left(\bar{\gamma}^2 d\tilde{t}^2 - \bar{h} d\tilde{x}^2\right) = 0\,. \tag{54}$$

The characteristics are equal to the high frequency limit for the acoustic macroscopic ($\pm\gamma_{\pi_+}(\infty)$) and optical microscopic ($\pm\gamma_{\pi_-}(\infty)$) phase velocities respectively defined later in this manuscript in equations (70).

3.2 Dispersion relation, phase and group velocities

Dispersion relation

As it is clearly illustrated by the equation of motion (50), the material's nonlinear behavior and its intrinsic microstructure lead to dispersive effects. We now carry out a dispersion analysis. We consider the general solution to the equation of motion (50) for a single non-dimensional harmonic wave propagating through a one-dimensional continuum with a velocity field of the form,

$$\hat{v}\left(\tilde{x},\tilde{t}\right)=e^{\imath\left(\kappa\tilde{x}-\varpi\tilde{t}\right)}\ , \tag{55}$$

where ϖ is the dimensionless frequency, and κ is the dimensionless wave number (number of wave-lengths per 2π). Substituting (55) into (50), yields the dispersion equation,

$$\left(1-\frac{\gamma_{0\mu}^{2}}{\bar{\gamma}^{2}}\right)\left[\kappa^{2}-\frac{\bar{h}}{\bar{\gamma}^{2}}\varpi^{2}\right]-\frac{1}{\bar{\gamma}^{2}}\frac{\gamma_{0\mu}^{2}}{\bar{\gamma}^{2}}\varpi^{2}-\frac{1}{\varepsilon_{\ell}^{2}}\left[\kappa^{2}-\frac{\bar{h}}{\bar{\gamma}^{2}}\varpi^{2}\right]\left[\frac{\gamma_{\mu}^{2}}{\rho_{\mu}}\kappa^{2}-h_{\mu}\varpi^{2}\right]=0\ . \tag{56}$$

Equation (56) has four solutions $\kappa=\pm\kappa_{\pm}\left(\varpi\right)$ with,

$$\kappa_{\pm}\left(\varpi\right)=\sqrt{\bar{\varphi}\left(\varpi\right)\pm\sqrt{\left[\bar{\varphi}\left(\varpi\right)\right]^{2}-\bar{\xi}\left(\varpi\right)}}\ , \tag{57}$$

or alternatively $\varpi=\pm\varpi_{\pm}\left(\kappa\right)$ such that,

$$\varpi_{\pm}\left(\kappa\right)=\sqrt{\bar{\phi}\left(\kappa\right)\mp\sqrt{\left[\bar{\phi}\left(\kappa\right)\right]^{2}-\bar{\zeta}\left(\kappa\right)}}\ . \tag{58}$$

The functions $\bar{\varphi}\left(\varpi\right)$, $\bar{\xi}\left(\varpi\right)$, $\bar{\phi}\left(\kappa\right)$ and $\bar{\zeta}\left(\kappa\right)$ are defined by

$$\bar{\varphi}\left(\varpi\right)=\frac{1}{2}\left(\frac{\bar{h}}{\bar{\gamma}^{2}}+\frac{\rho_{\mu}}{\gamma_{\mu}^{2}}h_{\mu}\right)\varpi^{2}+\frac{1}{2}\frac{\rho_{\mu}}{\gamma_{\mu}^{2}}\left(1-\frac{\gamma_{0\mu}^{2}}{\bar{\gamma}^{2}}\right)\varepsilon_{\ell}^{2}=f_{h}\varpi^{2}+\frac{1}{2}f_{\ell}\varepsilon_{\ell}^{2}\ , \tag{59}$$

$$\bar{\xi}\left(\varpi\right)=\frac{\rho_{\mu}}{\gamma_{\mu}^{2}}\frac{\bar{h}h_{\mu}}{\bar{\gamma}^{2}}\varpi^{2}\left(\varpi^{2}-\frac{1}{\bar{h}h_{\mu}}\left[\bar{h}\left(\frac{\gamma_{0\mu}^{2}}{\bar{\gamma}^{2}}-1\right)-\frac{\gamma_{0\mu}^{2}}{\bar{\gamma}^{2}}\right]\varepsilon_{\ell}^{2}\right)=g_{h}\varpi^{2}\left[\varpi^{2}-g_{\ell}\varepsilon_{\ell}^{2}\right]\ , \tag{60}$$

and,

$$\bar{\phi}\left(\kappa\right)=\frac{1}{2}\left(\frac{\bar{h}}{\bar{\gamma}^{2}}+\frac{\rho_{\mu}}{\gamma_{\mu}^{2}}h_{\mu}\right)\frac{\gamma_{\mu}^{2}}{\rho_{\mu}}\frac{\bar{\gamma}^{2}}{\bar{h}h_{\mu}}\kappa^{2}+\frac{1}{\bar{h}h_{\mu}}\left[\bar{h}\left(\frac{\gamma_{0\mu}^{2}}{\bar{\gamma}^{2}}-1\right)-\frac{\gamma_{0\mu}^{2}}{\bar{\gamma}^{2}}\right]\varepsilon_{\ell}^{2}=\frac{f_{h}}{g_{h}}\kappa^{2}+\frac{1}{2}g_{\ell}\varepsilon_{\ell}^{2}\ , \tag{61}$$

$$\bar{\zeta}\left(\kappa\right)=\frac{\gamma_{\mu}^{2}}{\rho_{\mu}}\frac{\bar{\gamma}^{2}}{\bar{h}h_{\mu}}\kappa^{2}\left[\kappa^{2}-\frac{\rho_{\mu}}{\gamma_{\mu}^{2}}\left(1-\frac{\gamma_{0\mu}^{2}}{\bar{\gamma}^{2}}\right)\varepsilon_{\ell}^{2}\right]=\frac{1}{g_{h}}\kappa^{2}\left[\kappa^{2}-f_{\ell}\varepsilon_{\ell}^{2}\right]\ . \tag{62}$$

The implicit coupling and convolution between microstructure and materials nonlinearity clearly appears in the above through the functions $\bar{\varphi}\left(\varpi\right)$ and $\bar{\xi}\left(\varpi\right)$ or alternatively through the functions

$\bar{\phi}(\kappa)$ and $\bar{\zeta}(\kappa)$. The dispersion relation (57) contains two distinct branches: the upper branch κ_+ (alternatively ϖ_+), also called the "acoustic" branch and the lower branch κ_- (alternatively ϖ_-), also called the "optical" branch. As we demonstrate later in section 3.3, both optical and acoustic branches can be expected given an arbitrary set of initial conditions.

Typical results for the dispersion relation (57) are presented in Figure 9 and compared to the linear elastic case [26]. Note that in the elastic case, the dispersion equation in the frequency domain takes the same form as in equation (57) with the functions $\bar{\varphi}(\varpi)$ and $\bar{\xi}(\varpi)$ being defined with their elastic counterparts $\bar{\varphi}^{el}(\varpi)$ and $\bar{\xi}^{el}(\varpi)$ (i.e. when h_0 and h_μ are both set to 1) such that,

$$\bar{\varphi}^{el}(\varpi) = \frac{1}{2}\left(\frac{1}{\bar{\gamma}^2} + \frac{\rho_\mu}{\gamma_\mu^2}\right)\varpi^2 + \frac{1}{2}\frac{\rho_\mu}{\gamma_\mu^2}\left(1 - \frac{\gamma_{0\mu}^2}{\bar{\gamma}^2}\right)\varepsilon_\ell^2 \text{ and } \bar{\xi}^{el}(\varpi) = \frac{1}{\bar{\gamma}^2}\frac{\rho_\mu}{\gamma_\mu^2}\varpi^2\left[\varpi^2 + \varepsilon_\ell^2\right] . \quad (63)$$

Similarly the dispersion equation in the wave number domain takes the same form as in equation (58) with the functions $\bar{\phi}(\kappa)$ and $\bar{\zeta}(\kappa)$ being defined with their elastic counterparts $\bar{\phi}^{el}(\varpi)$ and $\bar{\zeta}^{el}(\kappa)$ such that,

$$\bar{\phi}^{el}(\kappa) = \frac{1}{2}\left(\bar{\gamma}^2 + \frac{\gamma_\mu^2}{\rho_\mu}\right)\kappa^2 - \varepsilon_\ell^2 \text{ and } \bar{\zeta}^{el}(\kappa) = \bar{\gamma}^2\frac{\gamma_\mu^2}{\rho_\mu}\kappa^2\left[\kappa^2 - \frac{\rho_\mu}{\gamma_\mu^2}\left(1 - \frac{\gamma_{0\mu}^2}{\bar{\gamma}^2}\right)\varepsilon_\ell^2\right] . \quad (64)$$

Phase velocity

The dimensionless phase velocity $\gamma_\pi(\varpi) = \varpi/\kappa(\varpi)$ of the harmonic wave reads,

$$\gamma_{\pi\pm}(\varpi) = \frac{\varpi}{\sqrt{\bar{\varphi}(\varpi) \pm \sqrt{[\bar{\varphi}(\varpi)]^2 - \bar{\xi}(\varpi)}}} , \quad (65)$$

or alternatively $\gamma_\pi(\kappa) = \varpi(\kappa)/\kappa$ such that,

$$\gamma_{\pi\pm}(\kappa) = \frac{1}{\kappa}\sqrt{\bar{\phi}(\kappa) \mp \sqrt{\left[\bar{\phi}(\kappa)\right]^2 - \bar{\zeta}(\kappa)}} . \quad (66)$$

Typical results for the dimensionless phase velocity γ_π are plotted in Figure 10. The phase velocity γ_π depends on the frequency ϖ (wave number κ) and, consequently, wave propagation is dispersive for non-linear microstructured materials. As such, due to the fact that different harmonic waves propagate with different velocities, the shape of a pulse propagating through a microstuctured medium undergoes a change and a loading wave can potentially be transformed into a stationary localization wave. Note that from equation (66), the acoustic phase velocity remains real if

$$\kappa \geq \varepsilon_\ell \sqrt{\frac{\gamma_{0\mu}^2 + \Delta\gamma^2 - 2\gamma_{0\mu}\sqrt{\Delta\gamma^2}}{\left(\bar{\gamma}^2 - \frac{\gamma_\mu^2}{\rho_\mu}\right)^2}} \text{ with } \Delta\gamma^2 = \gamma_{0\mu}^2 - \bar{\gamma}^2 + \frac{\gamma_\mu^2}{\rho_\mu} . \quad (67)$$

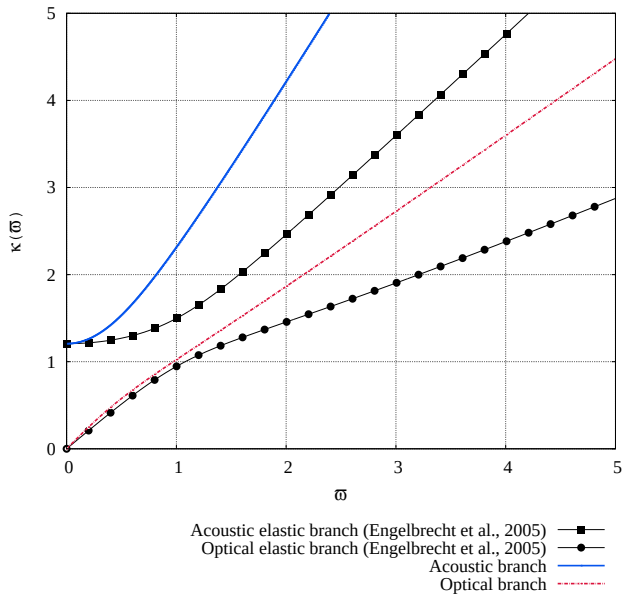

Figure 9. Dispersion relation for a hardening microstructured material following the equation of motion (40) with parameters $\gamma_\mu = 0.6$, $\gamma_{0\mu} = 1.6$, $\beta_{0\mu} = 1.3$, $\rho_\mu = 0.5$, $h_0 = 1.5$, $h_\mu = 3.0$ and $\varepsilon_\ell = 2.0$. Results illustrated in this figure are compared to the linear elastic case of equation (63) [26] for the same parameters.

Or equivalently,

$$\lambda \leq 2\pi\lambda_0 \ , \ \text{ with } \ \lambda_0 = \frac{1}{\varepsilon_\ell}\sqrt{\frac{\left(\bar{\gamma}^2 - \dfrac{\gamma_\mu^2}{\rho_\mu}\right)^2}{\gamma_{0\mu}^2 + \Delta\gamma^2 - 2\gamma_{0\mu}\sqrt{\Delta\gamma^2}}} \ , \tag{68}$$

where λ is the dimensionless wave length. The parameter λ_0 is an internal length scale associated with the microstructured medium. As such, no wavelength larger than $2\pi\lambda_0$ can fit within the microstructured medium potentially leading to a stationary harmonic localization wave with a width equal to $2\pi\lambda_0$. In other words, these waves are unstable and could grow unboundedly or decay. However, the localization region is limited by that critical wavelength and these waves can't occur. These results are consistent with those for the dispersive wave propagation in a gradient-dependent medium [101].

In the lower frequency range ($\varpi \to 0$), the acoustic phase velocity behaves similarly to the elastic phase velocity such that,

$$\gamma_{\pi+}(0) \approx \frac{\varpi}{\lambda_0} \approx \gamma_{\pi+}^{el}(\varpi) \ , \tag{69}$$

while the optical branch is undefined. In the higher frequency range ($\varpi \to \infty$), the acoustic and

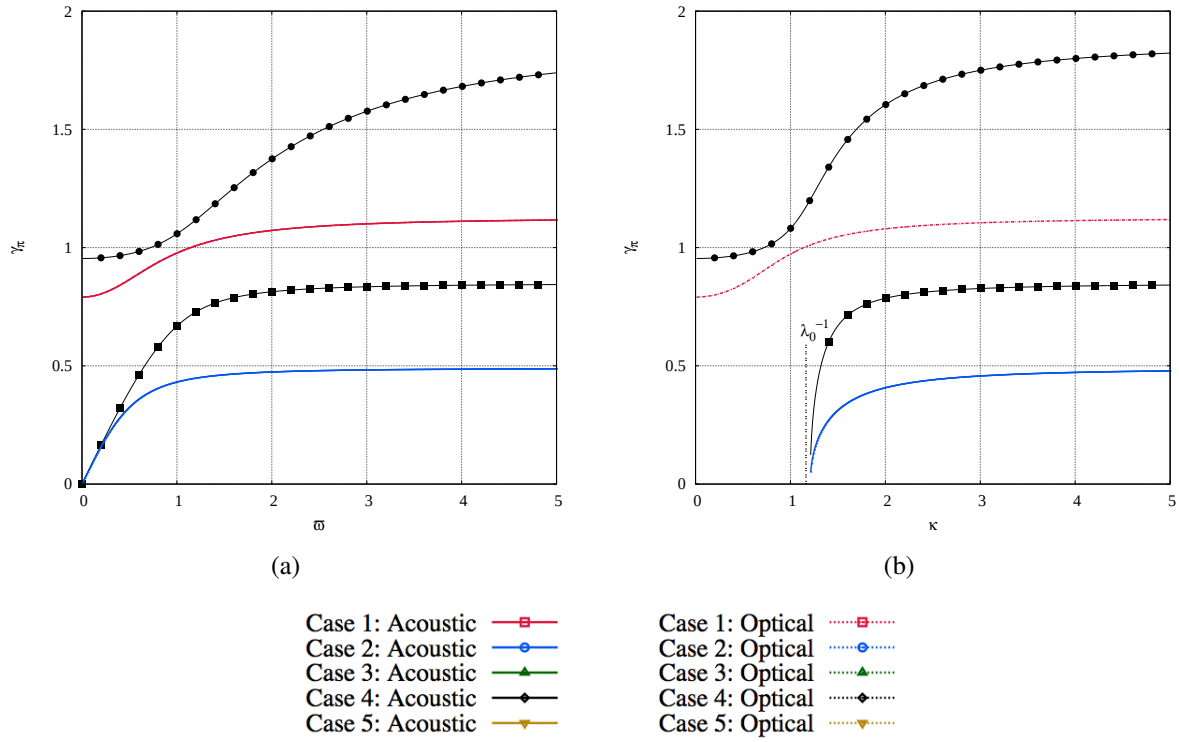

Figure 10. (a) Phase velocity−frequency relation and (b) Phase velocity−wave number relation for a hardening microstructured material using the parameters provided in Figure 9.

optical phase velocities tend to a macroscopically and microscopically defined limit respectively such that,

$$\gamma_{\pi+}(\infty) \approx \begin{cases} \sqrt{\dfrac{\bar{\gamma}^2}{\bar{h}}} & \text{if } \bar{h}\dfrac{\gamma_\mu^2}{\rho_\mu} \geq h_\mu \bar{\gamma}^2 \\ \sqrt{\dfrac{\gamma_\mu^2/\rho_\mu}{h_\mu}} & \text{if } \bar{h}\dfrac{\gamma_\mu^2}{\rho_\mu} \leq h_\mu \bar{\gamma}^2 \end{cases}, \tag{70a}$$

$$\gamma_{\pi-}(\infty) \approx \begin{cases} \sqrt{\dfrac{\gamma_\mu^2/\rho_\mu}{h_\mu}} & \text{if } \bar{h}\dfrac{\gamma_\mu^2}{\rho_\mu} \geq h_\mu \bar{\gamma}^2 \\ \sqrt{\dfrac{\bar{\gamma}^2}{\bar{h}}} & \text{if } \bar{h}\dfrac{\gamma_\mu^2}{\rho_\mu} \leq h_\mu \bar{\gamma}^2 \end{cases}, \tag{70b}$$

for $\left(h_0, h_\mu\right) \geq 1$. These limits correspond to the characteristics of the wave equation. The macroscopic hardening dominates the acoustic phase velocity while the microscopic hardening (for $\bar{h}\gamma_\mu^2/\rho_\mu \geq h_\mu \bar{\gamma}^2$) dominates the optical phase velocity. As illustrated in Figure 11, the characteristic microstructural length scale ε_ℓ accentuates the dispersive character for both the acoustic and optical branches.

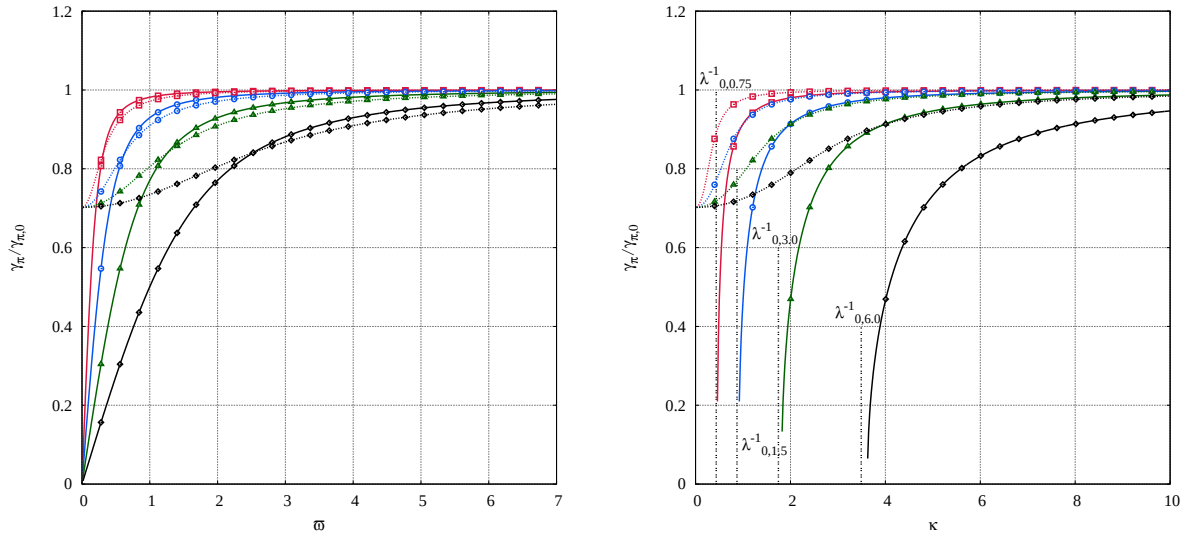

Figure 11. (a) Phase velocity−frequency relation and (b) phase velocity−wave number relation for a hardening microstructured material using the parameters provided in Figure 9 for various microstructural length scales ε_ℓ. Results are normalized by the phase velocity $\gamma_{\pi,0}$ when the characteristic microstructural length scale is infinitely small (i.e. microstructural effect can be neglected). Solid lines denote the acoustic branch, dotted lines denote the optical branch. Square symbols represent the phase velocity for $\varepsilon_\ell = 0.75$, round symbols represent the phase velocity for $\varepsilon_\ell = 1.5$, triangle symbols represent the phase velocity for $\varepsilon_\ell = 3.0$, and diamond symbols represent the phase velocity for $\varepsilon_\ell = 6.0$.

Group velocity

The dimensionless group velocity $\gamma_g(\varpi) = (d\kappa(\varpi)/d\varpi)^{-1}$ is given by,

$$\gamma_{g\pm}(\varpi) = \frac{2\kappa_\pm(\varpi)}{\bar{\gamma}'(\varpi)\pm\dfrac{\bar{\gamma}'(\varpi)\bar{\gamma}(\varpi)-\dfrac{1}{2}\bar{\xi}'(\varpi)}{\sqrt{[\bar{\gamma}(\varpi)]^2-\bar{\xi}(\varpi)}}}\,, \tag{71}$$

where " $'$ " denotes the derivative with respect to ϖ. For example $\bar{\gamma}' = d\bar{\gamma}/d\varpi$. Alternatively $\gamma_g(\kappa) = d\varpi(\kappa)/d\kappa$ is given by,

$$\gamma_{g\pm}(\kappa) = \frac{\bar{\phi}'(\kappa)\mp\dfrac{\bar{\phi}'(\kappa)\bar{\phi}(\kappa)-\dfrac{1}{2}\bar{\zeta}'(\kappa)}{\sqrt{\left[\bar{\phi}(\kappa)\right]^2-\bar{\zeta}(\kappa)}}}{2\varpi_\pm(\kappa)}\,, \tag{72}$$

where in this case " $'$ " denotes the derivative with respect to κ. Group velocity is the velocity of the modulation of a packet of waves were there is significant scale separation between the wavelength of the waves in the "packet" and that of the modulation. In this way, group velocity can be thought of as the velocity at which energy is propagated. Typical results for the dimensionless group velocity γ_g are plotted in Figure 12.

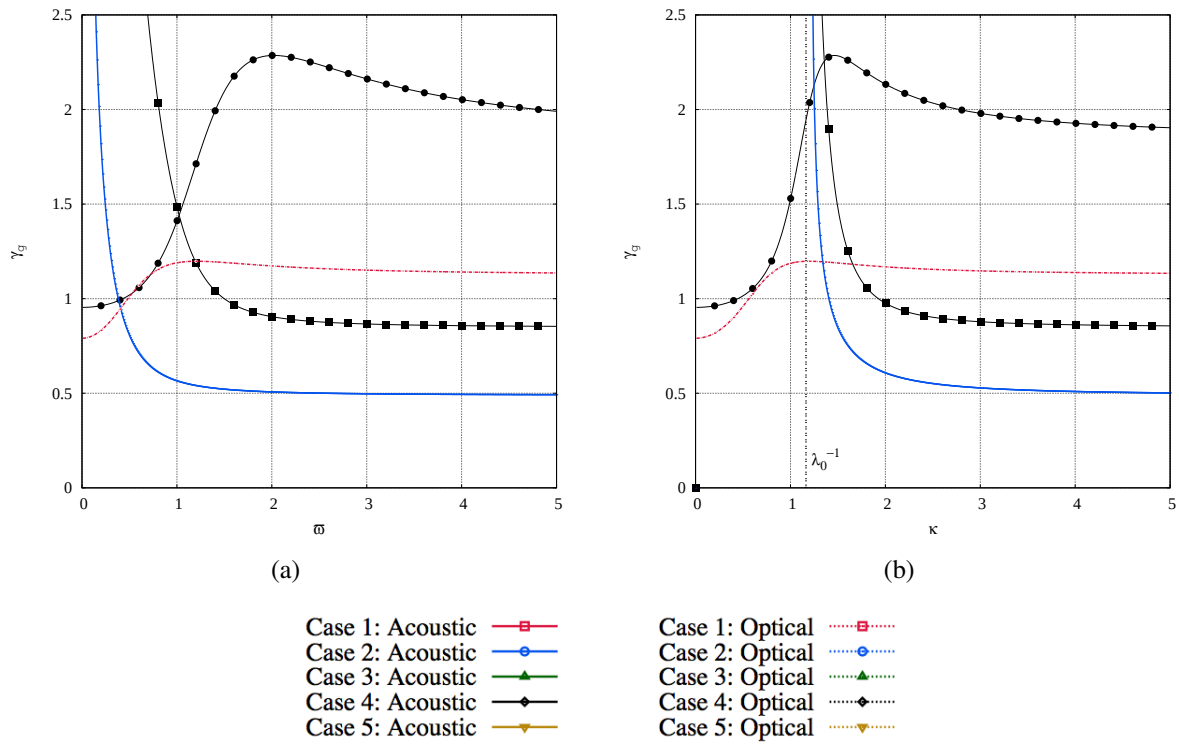

Figure 12. (a) Group velocity−frequency relation and (b) Group velocity−wave number relation for a hardening microstructured material using the parameters provided in Figure 9.

Again, as illustrated in Figure 13, the characteristic microstructural length scale ε_ℓ accentuates the dispersive character for both the acoustic and optical branches.

3.3 Discussion

Influence of microstructural features on the dispersive character

It is clearly seen through the dispersion relation, the phase and group velocity relations that the values of the material constants (both elastic and plastic) and the microstructural length scale ε_ℓ in the governing differential equation (50) play an important part in dictating the type of wave

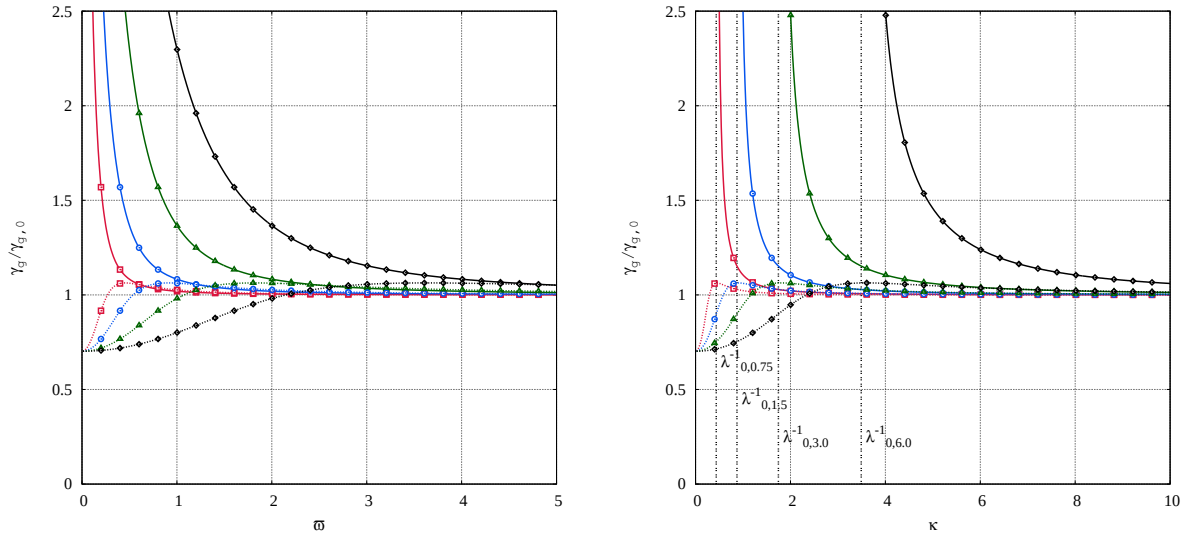

(a) (b)

Figure 13. (a) Group velocity−frequency relation and (b) group velocity−wave number relation for a hardening microstructured material using the parameters provided in Figure 9 for various microstructural length scales ε_ℓ. Results are normalized by the group velocity $\gamma_{g,0}$ when the characteristic microstructural length scale is infinitely small (i.e. microstructural effect can be neglected). Solid lines denote the acoustic branch, dotted lines denote the optical branch. Square symbols represent the phase velocity for $\varepsilon_\ell = 0.75$, round symbols represent the phase velocity for $\varepsilon_\ell = 1.5$, triangle symbols represent the phase velocity for $\varepsilon_\ell = 3.0$, and diamond symbols represent the phase velocity for $\varepsilon_\ell = 6.0$.

propagation in the microstructured medium. Figure 14 illustrates the influence of some of the input parameters used in the model, namely the micro-elasticity scaling factor $\beta_{0\mu}$, the coupling term between the micro- and macrodeformation $\gamma_{0\mu}$, the macroscopic hardening ($h_0 > 1$)/softening ($h_0 < -1$) modulus, and the microscopic hardening ($h_\mu > 1$)/softening ($h_\mu < -1$) modulus on the dispersion relation, the phase velocity and group velocity. For example, is it illustrated that, when the coupling between the micro- and macrodeformation is ignored ($\gamma_{0\mu} = 0$), a drastically different dispersion relation and phase velocity and group velocity is observed. In this case, the acoustic and optical wave intersect each other corresponding to discontinuity point in the dispersion curves. After that point the optical becomes continuous with the lower branch (low values of κ) of the acoustic branch and similarly the acoustic branch becomes continuous with the lower branch of the optical branch. Such analysis could be useful to define a viable material constants input space for with the solutions are physically acceptable. A full discussion on the influence of the materials parameters and their physical relevance on the wave propagation properties is beyond the scope of this manuscript. Recent work by the authors [22] provides additional discussion on how these parameters can be extracted from mesoscale *Direct Numerical Simulation* (simulations in which

the microstructural topology is explicitly resolved in the spatial discretization).

Another interesting aspect on the importance of the materials parameters on the type of wave propagation occurring in the microstructured medium is for the case when $[\bar{\varphi}(\varpi)]^2 - \bar{\xi}(\varpi) = 0$ or equivalently for,

$$\varpi = \varpi_{\pm\text{cut-off}} = \varepsilon_\ell \sqrt{\Pi \pm \sqrt{\Pi^2 - \Upsilon}} \,, \tag{73}$$

with the function Π and Υ defined as,

$$\Pi = \frac{1}{\bar{h}\dfrac{\gamma_\mu}{\rho_\mu} - h_\mu \bar{\gamma}^2} \left[\frac{2\gamma_\mu^2 \gamma_{0\mu}^2}{\bar{h}\dfrac{\gamma_\mu}{\rho_\mu} - h_\mu \bar{\gamma}^2} + \bar{\gamma}^2 - \gamma_{0\mu}^2 \right] \,, \tag{74a}$$

$$\Upsilon = \left(\frac{\bar{\gamma}^2 - \gamma_{0\mu}^2}{\bar{h}\dfrac{\gamma_\mu}{\rho_\mu} - h_\mu \bar{\gamma}^2} \right)^2 \,. \tag{74b}$$

This cut-off frequency $\varpi_{\pm\text{cut-off}}$ [41] corresponds to the frequency after which a potential unstable mode (for a given set of materials parameters rendering equation (57) imaginary) becomes a propagating mode and therefore changing the wave behavior.

Comparison with a gradient-dependent model

To illustrate the properties of the model developed in section 3.1, the dispersion curves, phase velocity curves and group velocity curves obtained in section 3.2 are compared with a continuum model that incorporates a dependence upon the Laplacian of the inelastic strain [101]. Using the same convention defined to derive equation (50), the non-dimensionalized wave equation (see equation (24) in [101]) for a gradient-dependent model reads:

$$h_0 v_{\tilde{t}\tilde{t}} - v_{\tilde{x}\tilde{x}} + \frac{c_s (h_0 - 1)}{\varepsilon_\ell^2} \left[v_{\tilde{x}\tilde{x}\tilde{x}\tilde{x}} - v_{\tilde{x}\tilde{x}\tilde{t}\tilde{t}} \right] = 0 \,, \tag{75}$$

where the normalized coefficients (h_0, c_s) are defined based on the coefficients $(h, \bar{c})$ defined in equations (10) and (11) in [101] such that,

$$h = \frac{E_0}{h_0 - 1} \quad \text{and} \quad \bar{c} = c_s E_0 \bar{\ell}^2 \,, \tag{76}$$

where E_0, h_0 and $\bar{\ell}^2$ are defined earlier in this manuscript.

Following the dispersion analysis presented in section 3.2, the dispersion relation for the gradient-dependent model in equation (75) is given by,

$$\varpi_\pm(\kappa) = \kappa \sqrt{\frac{1 - \dfrac{c_s(1 - h_0)}{\varepsilon_\ell^2}\kappa^2}{h_0 - \dfrac{c_s(1 - h_0)}{\varepsilon_\ell^2}\kappa^2}} \,, \tag{77}$$

or alternatively,

$$\kappa_{\pm}(\varpi) = \sqrt{\varphi_s(\varpi) \pm \sqrt{[\varphi_s(\varpi)]^2 - \xi_s(\varpi)}}\,, \tag{78}$$

with,

$$\varphi_s(\varpi) = \frac{1}{2}\left(\varpi^2 + \varepsilon_\ell^2 \frac{1}{c_s(1-h_0)}\right) \text{ and } \xi_s(\varpi) = \varepsilon_\ell^2 \frac{h_0}{c_s(1-h_0)}\varpi^2. \tag{79}$$

Comparison of the dispersion relation (77) with the dispersion relation (58) is shown in Figure 15 (a).

The phase velocity for the gradient dependent model is subsequently given by,

$$\gamma_{\pi\pm}(\kappa) = \sqrt{\frac{1 - \dfrac{c_s(1-h_0)}{\varepsilon_\ell^2}\kappa^2}{h_0 - \dfrac{c_s(1-h_0)}{\varepsilon_\ell^2}\kappa^2}} \text{ and } \gamma_{\pi\pm}(\varpi) = \frac{\varpi}{\sqrt{\varphi_s(\varpi) \pm \sqrt{[\varphi_s(\varpi)]^2 - \xi_s(\varpi)}}}\,. \tag{80}$$

Similarly to what was noted in section 3.2, the acoustic phase velocity for the gradient-dependent model remains real if the dimensionless wave length λ satisfies

$$\lambda \leq 2\pi\lambda_0 \text{ with } \lambda_0 = \frac{1}{\varepsilon_\ell}\sqrt{c_s(1-h_0)}\,. \tag{81}$$

The group velocity for a gradient-dependent model reads,

$$\gamma_{g\pm}(\kappa) = \frac{\kappa}{\varpi_{\pm}(\kappa)}\left[1 + \frac{h_0(1-h_0)}{\left(h_0 - \dfrac{c_s(1-h_0)}{\varepsilon_\ell^2}\kappa^2\right)^2}\right]\,, \tag{82}$$

or alternatively

$$\gamma_{g\pm}(\varpi) = \frac{2\kappa_{\pm}(\varpi)}{\bar{\varphi}_s'(\varpi) \pm \dfrac{\bar{\varphi}_s'(\varpi)\,\bar{\phi}_s(\varpi) - \dfrac{1}{2}\bar{\xi}_s'(\varpi)}{\sqrt{[\bar{\varphi}_s(\varpi)]^2 - \bar{\xi}_s(\varpi)}}}\,, \tag{83}$$

where " $'$ " denotes the derivative with respect to ϖ. Comparisons of the phase and group velocities between the gradient-dependent model and the model described in the present manuscript are shown in Figure 15 (b) and (c) respectively.

As it is illustrated in Figure 15, the present micromorphic model for a hardening microstructured material is in good agreement with the gradient-dependent macroscopic model. It is interesting to note that various combinations of the micromorphic materials parameters could yield to a similar fit to the gradient-dependent model. Again, a full discussion on the most appropriate materials parameters to be used in the micromorphic model for the comparison with the gradient-dependent model is beyond the scope of this manuscript. Rather it should be noted that, similarly

to a gradient-dependent continuum model, in our micromorphic model composed of a simple plasticity model both at the macro- and microscale, the phase speed does not necessarily become imaginary at the onset of softening, as it is the case in classical continuum models. The dispersive character of such models "forces" strain softening regions to localize [101].

Partitioning amongst optical and acoustic phase-speeds

In the analysis of section 3.2 it is seen that four phase-speeds may be excited in the solution of equation (50). Specifically, all solutions include forward and backward going acoustic and optical phase-speeds (ϖ_{a+}, ϖ_{a-}, ϖ_{o+} and ϖ_{o-} respectively). Here we briefly describe how initial conditions determine the excitation of these components.

Begin by noting that the full (homogeneous) solution to equation (50) may be written as,

$$v(\tilde{x},\tilde{t}) = \sum_{\kappa=0}^{\infty} v_\kappa(\tilde{x},\tilde{t}) \tag{84}$$

with,

$$\begin{aligned} v_\kappa(\tilde{x},\tilde{t}) &= C_{a^+,\kappa}\left[\exp\left(\imath\kappa\tilde{x} - \varpi_{a^+}\tilde{t}\right)\right] \\ &+ C_{a^-,\kappa}\left[\exp\left(\imath\kappa\tilde{x} - \varpi_{a^-}\tilde{t}\right)\right] \\ &+ C_{o^+,\kappa}\left[\exp\left(\imath\kappa\tilde{x} - \varpi_{o^+}\tilde{t}\right)\right] \\ &+ C_{o^-,\kappa}\left[\exp\left(\imath\kappa\tilde{x} - \varpi_{o^-}\tilde{t}\right)\right]. \end{aligned} \tag{85}$$

For the fourth order wave equations, four initial conditions are needed. Taking the first four temporal derivatives of eqaution (84), setting them equal to their associated (specified) initial conditions, multipling them against $\exp(-\imath n\tilde{x})$, and integrating over $-\pi$ to π yields the system,

$$\begin{bmatrix} \mathscr{F}_\kappa(f_0) \\ \mathscr{F}_\kappa(f_1) \\ \mathscr{F}_\kappa(f_2) \\ \mathscr{F}_\kappa(f_3) \end{bmatrix} = \begin{bmatrix} 1 & 1 & 1 & 1 \\ -\imath\varpi_{a^+} & \imath\varpi_{a^-} & -\imath\varpi_{o^+} & \imath\varpi_{o^-} \\ -\varpi_{a^+}^2 & -\varpi_{a^-}^2 & -\varpi_{o^+}^2 & -\varpi_{o^-}^2 \\ \imath\varpi_{a^+}^3 & -\imath\varpi_{a^-}^3 & \imath\varpi_{o^+}^3 & -\imath\varpi_{o^-}^3 \end{bmatrix} \begin{bmatrix} C_{a^+,\kappa} \\ C_{a^-,\kappa} \\ C_{o^+,\kappa} \\ C_{o^-,\kappa} \end{bmatrix} \tag{86}$$

where,

$$\mathscr{F}_\kappa(f_i) = \frac{1}{2\pi}\int_{-\pi}^{\pi} f_i(\tilde{x})\exp(-\imath\tilde{x}\kappa)d\tilde{x} \tag{87}$$

are the Fourier coefficients (for wave-number κ) of the imposed initial condition i^{th} temporal derivatives. Note that f_1 is in general not $f_{0\tilde{t}}$, etc. Equation (86) is solved for the amplitudes, C, for each of the four phase-speeds, for each wave-number in all the initial conditions, f_i. Additionally, recall that as the problem is linear, each κ solution is independent of all others. It is evident from equation (86) that given arbitrary initial conditions, all phase-speeds will be present for all active wave-numbers.

3.4 Conclusions of Dispersion Analysis

This paper presents a 1D microcontinuum model that incorporates both a dependence upon the microstructure and inelastic behavior that is used to study wave dispersion in nonlinear, microstruc-

tured media. This microcontinuum model is based on the mechanics of generalized continua and introduces characteristic parameters (characteristic microstructural length scale and microstructural materials parameters) arising from the inhomogeneous behavior of the microstructure. These parameters are generally related to microstructural features. Nonlinearity is introduced in this study only through the description of the yield surfaces during plastic deformation both at the macroscopic and microscopic level. Several conclusions can be drawn from this work including:

- The introduction of inelastic behavior clearly impacts the phase speed behavior of the micromorphic material response. We see that depending on the coupling between the macroscale and the microscale, the dispersive character of the medium can drastically changes. Careful attention should be paid to the correlation between the dispersive character of the microstructured medium and the associated materials properties.

- This model includes as a subset, that of [26] when hardening parameters are set appropriately, i.e. in the case of a linear elastic microcontinuum $\left(h_0, h_\mu\right)$. Our analysis also includes as a subset, that of [101] for a gradient-dependent model, and it was shown that an "exclusion" zone can develop in the medium where waves do not propagate but may grow or decrease in amplitude with time (unstable wave).

- Mathematically speaking, the following approach overcome the ill-posedness of the set of partial differential equations governing the wave propagation. It has been shown that the introduction of an internal length scale regularizes the problem and the wave propagation in the micromorphic medium is well-posed for a careful choice of materials parameters. Choice of these parameters is beyond the scope of this manuscript but as mentioned in a previous study [22], *Direct Numerical Simulation* could be used to spatially resolve the complexity and richness of a wave propagating through microstructured heterogeneous media and and calibrate such micromorphic models.

- In general, all phase-speeds, including those of the acoustic and optical branches, are present in a solution. Other authors note the presence of the optical-branch in their phase speed analysis but ignore its impact when demonstrating analytical solutions to arbitrary input waves. To our knowledge we are the first to demonstrate the partitioning between these branches.

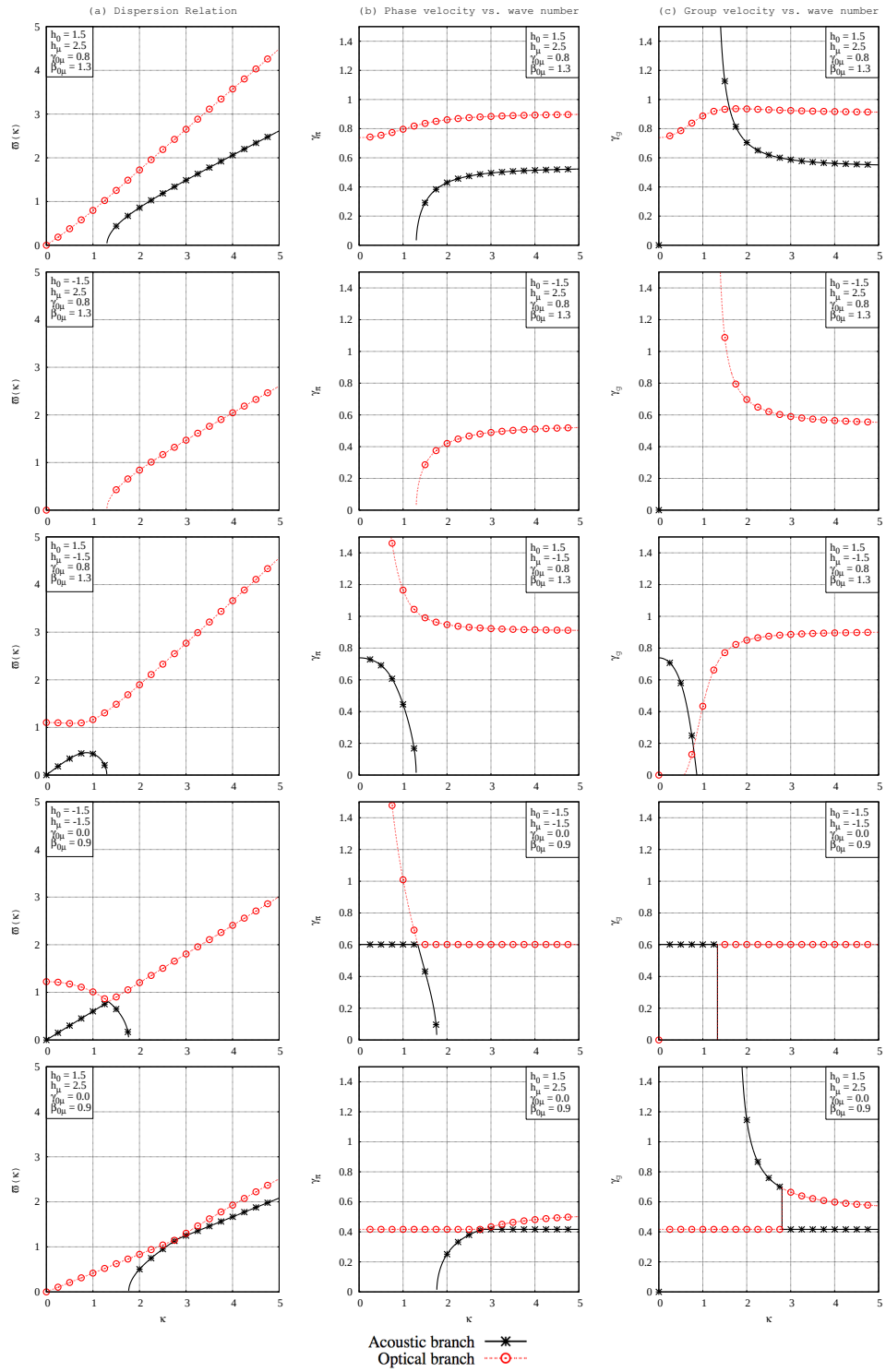

Figure 14. Impact of the macro-/microscopic materials constants on (a) dispersion relation, (b) phase velocity−wave number relation and (c) group velocity−wave number relation. Solid lines denote the acoustic branch, dotted lines the optical branch. Parameters common to all cases are $\gamma_\mu = 0.6$, $\rho_\mu = 0.5$ and $\varepsilon_\ell = 2.0$. The macro-/micro- hardening parameters (h_0/h_μ), coupling term ($\gamma_{0\mu}$) and micro-elasticity scaling factor ($\beta_{0\mu}$) are annotated for each case.

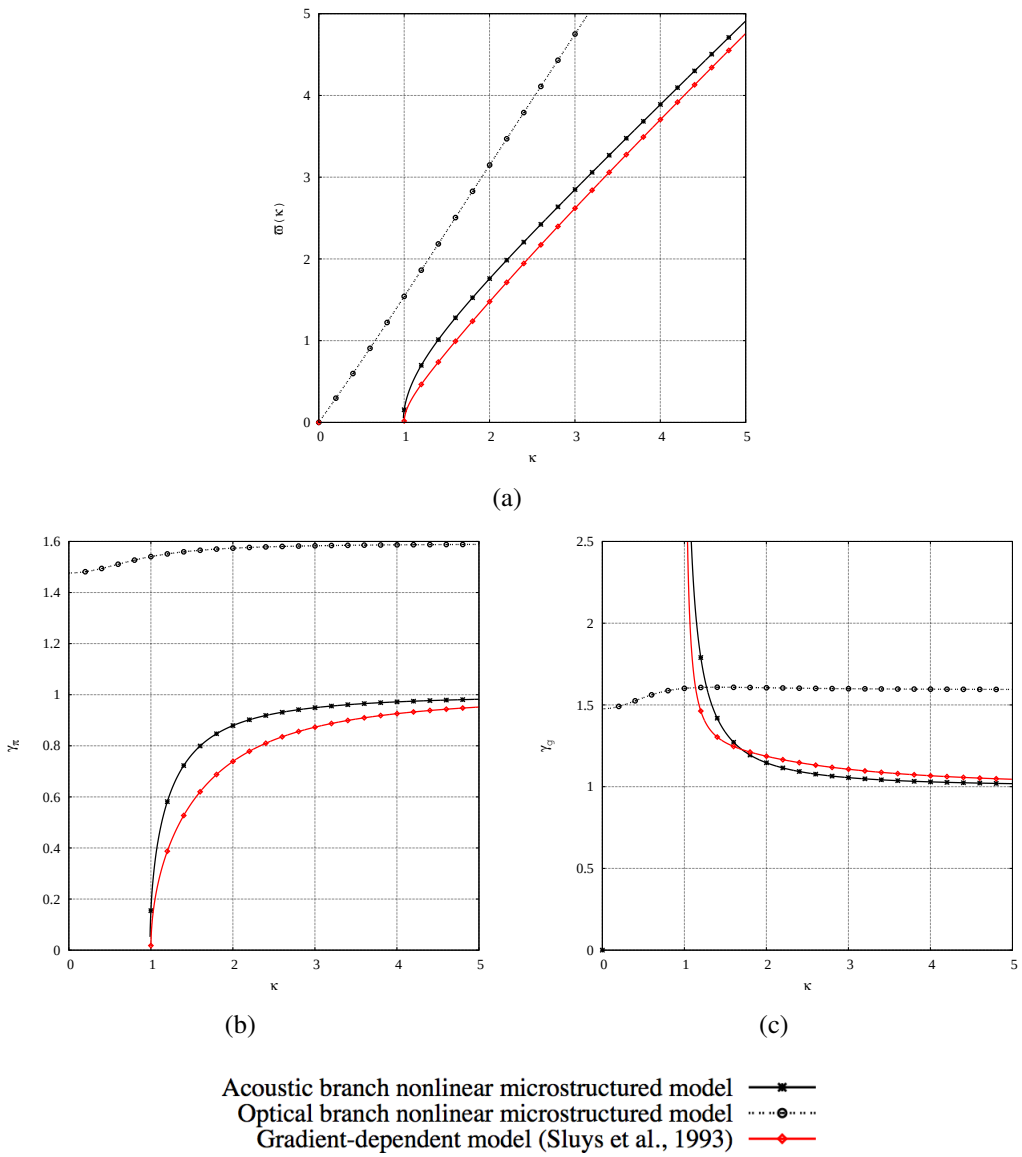

Figure 15. Comparison between a hardening microstructured material model and a gradient-dependent hardening material [101] for (a) Dispersion relation, (b) phase velocity−wave number relation, and (c) group velocity−wave number relation. Parameters used for the micromorphic hardening model are adapted from [101] such that $\gamma_\mu = 2$, $\rho_\mu = 1$, $\gamma_{0\mu} = 0.086$, $\beta_{0\mu} = 0.9$, $h_0 = -1.5$ and $h_\mu = 2.0$ and $\varepsilon_\ell = 2.0$. Parameters for the gradient dependent model are $h_0 = -1.5$, $\varepsilon_\ell = 2.0$ and $c_s = 1.6$.

4 Velocity Dispersion Experiments (DICE shots 242-244)

The goal of these experiments was to measure velocity dispersion due to (fcc) copper material heterogeneity in a gas gun shot and to establish an upper boundary on such dispersion (Figure 16). In the following, $[m : n]$ represents the widths of a bell curve with a half-max half-width of m (m/s) and near-toe half-width of n (m/s). For impact of a thin (0.4 mm) plate of annealed copper on a copper plate (3 mm thick) at 350 - 400 m/s, predictions show heterogeneity-caused velocity dispersion of [3:8] during the release (which has a slope of -1 m/s per ns). However, data from

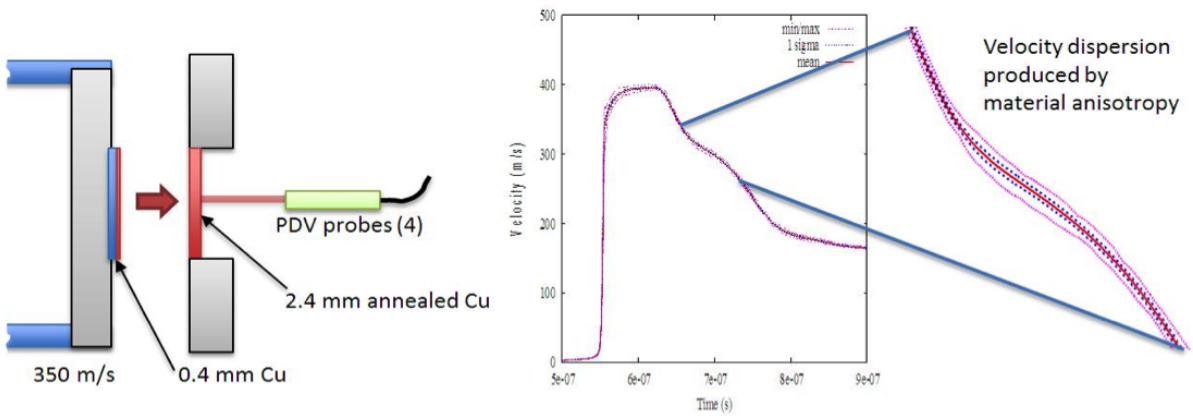

Figure 16. General concept for DICE gas gun shots 242-244.

copper bicrystal shots at lower impact velocities ([100] and [124] orientations) showed velocity deviations of several times this, together with strong side-running waves (reshocks/releases) apparently caused by the material anisotropy (Figure 17). This suggested the numerical predictions might be low.

4.1 Configuration

Two shots were performed with annealed copper samples ($40\mu m$ grains) and one with an aluminum sample (which should show weaker velocity dispersion due to the nearly isotropic single crystal response), using four probes on each of the copper shots and two on the aluminum shot. The copper was supplied by G. T. Gray III (LANL). Preshot calculations indicated that the shots might or might not show positive evidence of velocity dispersion.

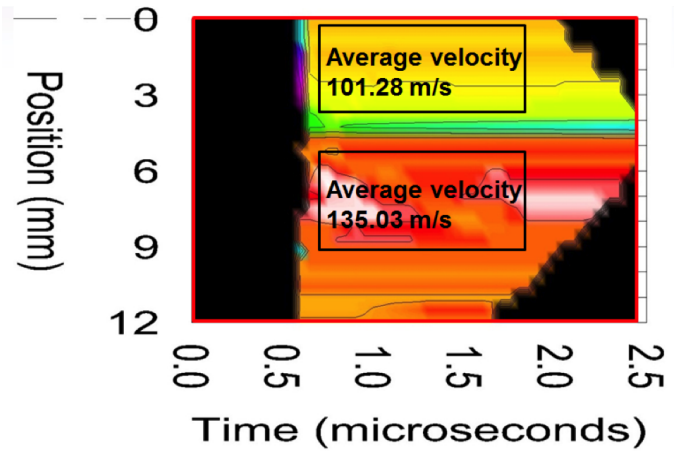

Figure 17. Velocity field from copper impacting copper bicrystal windowed by Z-cut quartz (DICE gas gun shot 199).

Tilt

While the impact tilt was expected to be less than one milliradian, portions of the very-thin copper impactor plates were not flat, with tilts ranging up to 4 milliradians. With a 350 m/s impact and a 300 μm diameter PDV probe spot size, this could cause a 3.4 ns arrival time spread, corresponding to an 3.4 m/s observed velocity spread during the release, comparable to the expected dispersion.

FFT Window Limits

In most PDV analyses, the peak of the spectral distribution is of most interest. Here it is the width. As increased time resolution is demanded via narrower timeslices, the width of the spectral amplitude peak increases (Figure 18). This proved to be the most important limitation for measuring velocity dispersion. For the present problem, simulations of the PDV signal (some performed prior to the shots, others during the execution and afterward) showed that distinguishing the predicted velocity dispersion from a single-velocity behavior would require a constant-velocity region of the velocity history at least 102.4 ns long. If the dispersion is doubled, this figure drops to 51.2 ns. On the chance that larger values of [12,32] are applicable, a window of 25.6 ns would work, which would be usable on the release. These limits reflect intrinsic broadening of amplitude-versus-velocity peaks calculated from original PDV data (Figure 18), windowed with Hamming windows and processed via Fourier transform.

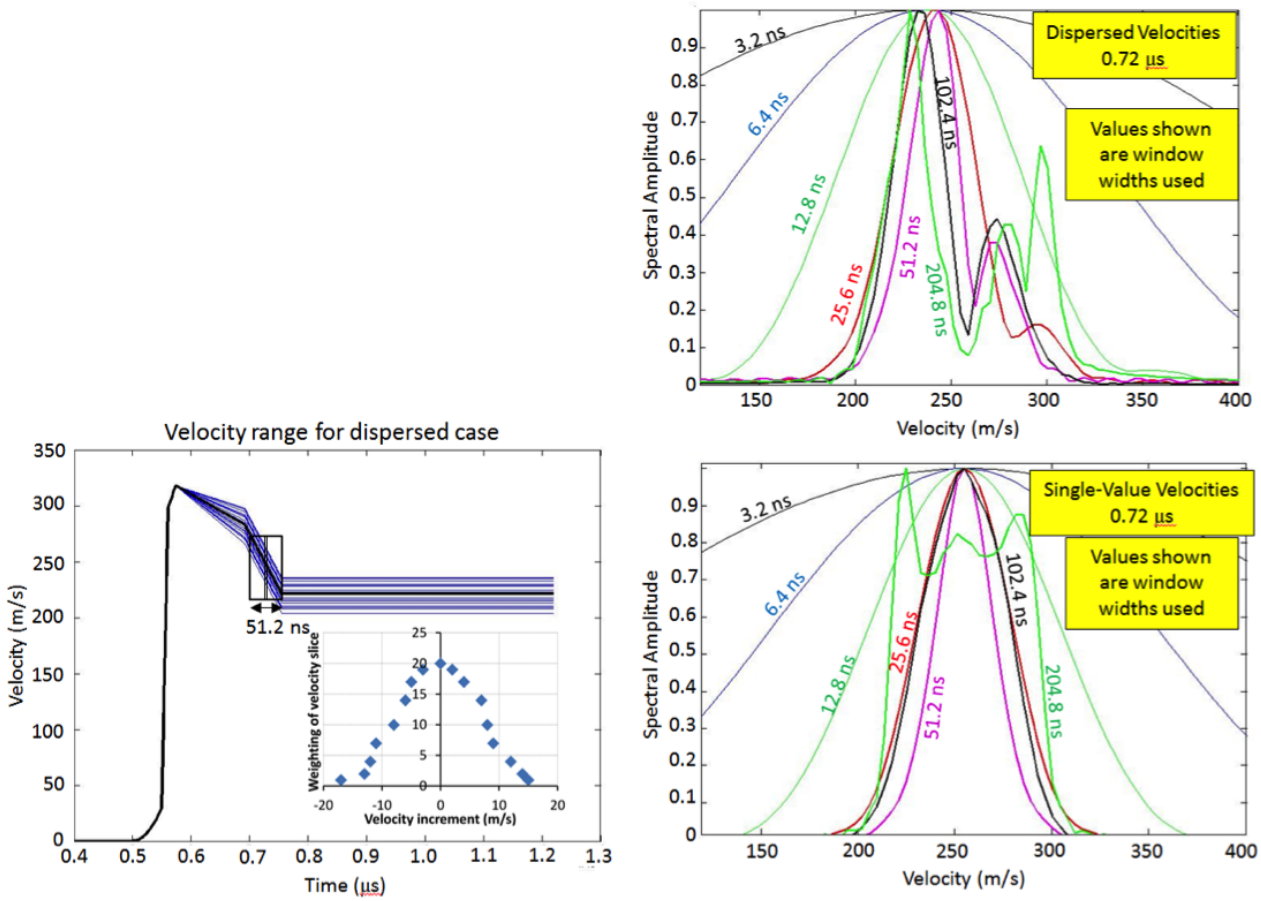

Figure 18. Padded transforms for simulated copper experiment with a variety of sliding FFT window widths, taken at the time noted on the synthetic trace.

4.2 Shot Details

Three shots were conducted on the DICE gas gun. Shots 242 and 243 followed the blueprint of Figure 16. It was originally planned to soft-recover the copper target plates, re-machine them and shoot them again to compare the response of annealed copper and cold-worked copper. However, the soft recovery hardware was not available in time for these shots.

Shot 242

A photo of the shot hardware is shown in Figure 19. An innovative adjustable probe holder was built to accommodate the required four PDV probes. The copper impactor was found to have too much localized tilt due to machining of the underlying PMMA, so a new projectile was constructed

with the copper impactor resting directly on the projectile nosetip. The impactor thickness was 0.3997 mm, while the copper target thickness was 3.1224 mm. Four collimating PDV probes were used (three with a nominal 0.95 mm diameter collimated beam and one with a nominal 0.22 mm diameter beam). The beam sizes were verified with a beam profilometer and found to be within 10% of nominal. The 0.22 mm probe returned good quality PDV data while the larger diameter probes surprisingly did not. Data were acquired on an Agilent Infiniuum digitizer (25 MHz, 80 GS/s). The shot was conducted with an impact velocity of 0.331 km/s. The overall tilt was slightly less than 1.2 milliradians.

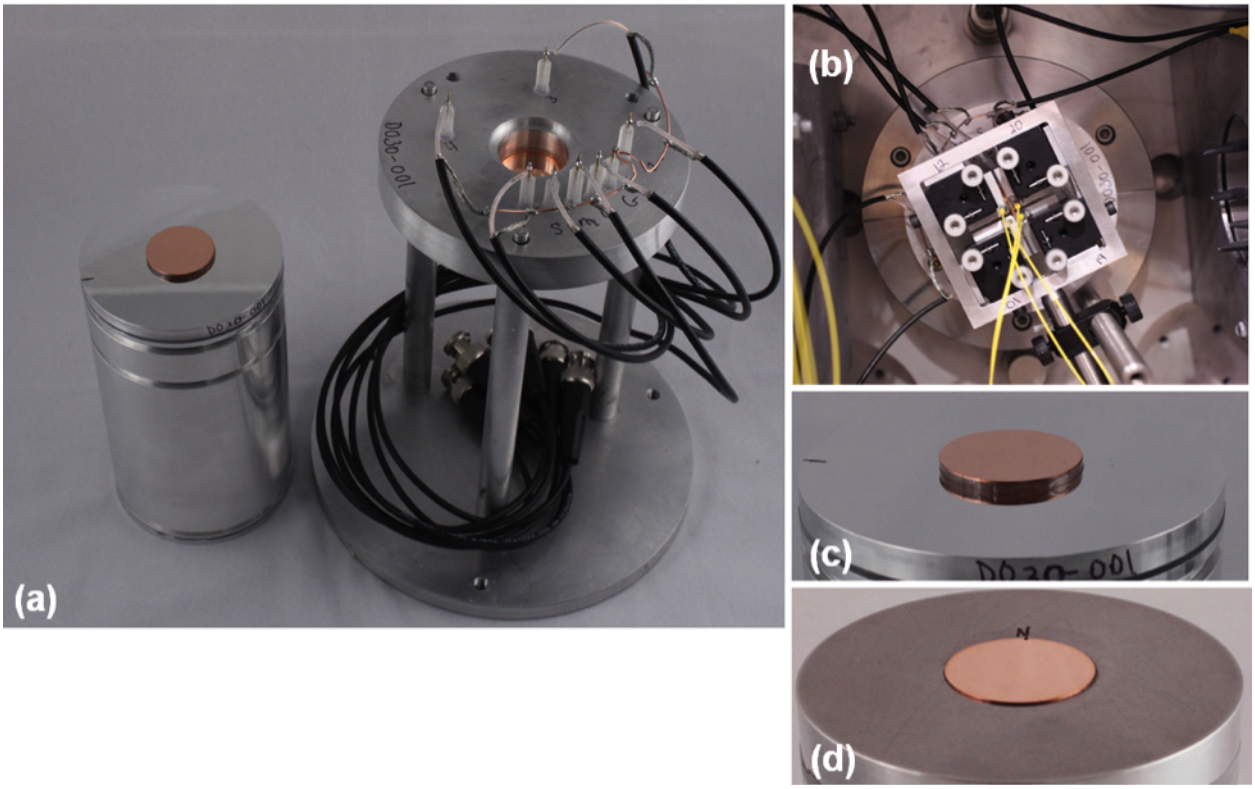

Figure 19. . Shot 242 hardware. (a) Overall, (b) PDV probe holder, (c) nosetip with PMMA under copper (not used), (d) nosetip with aluminum under copper (used).

Shot 243

This was identical to Shot 242 except as follows. The copper impactor thickness was 0.3984 mm and the target thickness was 3.1231 mm (both were one inch diameter). The impact velocity was 0.332 km/s.

Shot 244

A 1060 aluminum target 2.007 mm thick and 12.07 mm in diameter was used (very low crystalline anisotropy). The copper impactor thickness was 0.3984 mm and the target thickness was 3.1231 mm (both were one inch diameter). The impact velocity was 0.333 km/s. Two 22 micron PDV probes were used.

4.3 Results

The copper shot data showed a minimum peak width of [16:50] for a 51.2 ns window, both for the beginning and the middle of the steepest release. This may be due primarily to the overall surface acceleration during that time (Figure 20). The Al shot data showed a [14:27] peak for the

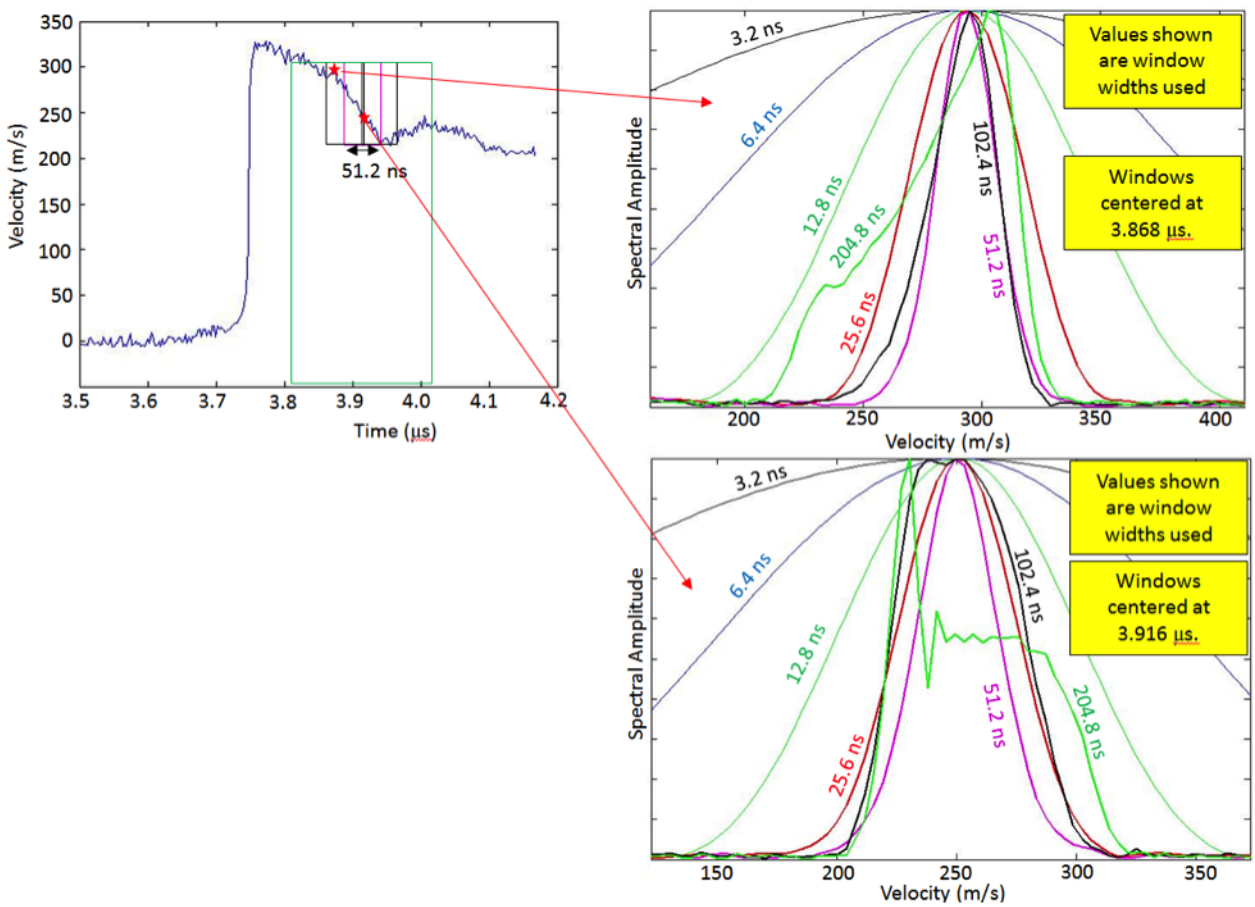

Figure 20. Padded transforms for DICE gas gun shot 243 (probe 1 data). Two different times are analyzed, with various FFT window widths.

zero-acceleration plateau (51.2 ns FFT window). Simulations showed the same widths for a non-dispersive surface and a [19:40] peak for a surface with velocity dispersion of [12:32] (Figure 21).

These analyses and models used zero-padded Hamming windowed portions of the PDV data (padded to 16,358 points, or 204.8 ns) to smooth the spectral amplitude peaks. Attempts to glean better constraints by other methods such as windowing a repeated sequence of portions of the data or randomizing starting phases of the light for the separate reflectors (different velocities) have not improved the velocity resolution.

4.4 Conclusions of Experimental Work

The velocity dispersion on the release of the copper experiments does not exceed a 1-sigma value of 12 m/s. Unfortunately, this is a relatively weak constraint in view of the original prediction of a 1-sigma value of 3 m/s. However, it does rule out the much larger deviations that appeared credible from the earlier copper bicrystal work.

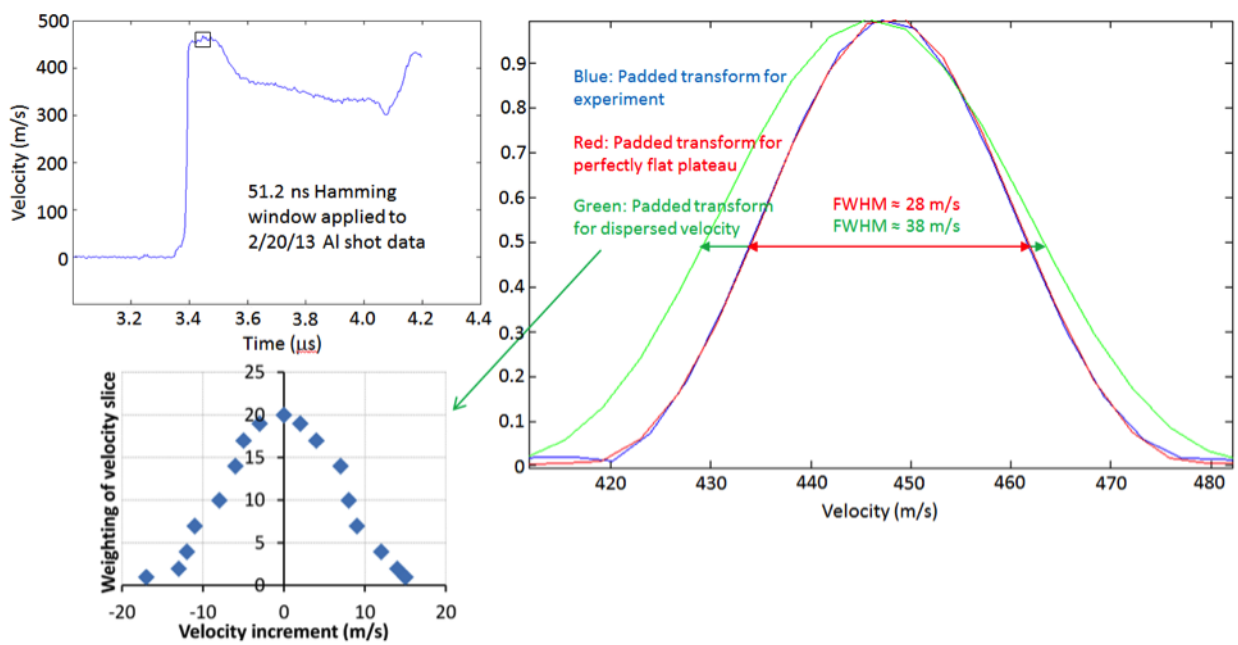

Figure 21. Padded transforms for Al experiment, flat plateau and plateau with noted velocity dispersion

Future work

The following are additional ways to characterize the effect of crystalline anisotropy on shock propagation:

1. Look for impact configurations where crystalline anisotropy would be expected to produce velocity dispersion on a less-accelerated part of the waveform (e.g. a plateau greater than 103 ns long).

2. Use fiber optic ribbons imaged onto the surface with spot sizes less than 20 microns (0.5x the average grain size), providing signal to a large number of VISAR channels. This would result in a statistical distribution of velocities, and would be usable on accelerating surfaces such as in the present experiment. It should be sensitive to the 2 m/s level. Other options may arise upon further investigation. This problem appears to be of increasing importance in the material dynamics field with progressively more stringent requirements for prediction of dynamic behavior of materials and the use of more exotic materials.

References

[1] J. D. Achenbach. *Wave Propagation in Elastic Solids*. Elsevier Science Publishers BV, Amsterdam, 1999.

[2] J. R. Allegra and S. A. Hawley. Attenuation of sound in suspensions and emulsions: Theory and experiments. *The Journal of the Acoustical Society of America*, 51(5B):1545–1564, 1972.

[3] Igor V Andrianov, Vladimir I Bolshakov, Vladyslav V Danishevs'kyy, and Dieter Weichert. Higher order asymptotic homogenization and wave propagation in periodic composite materials. *Proceedings of the Royal Society A: Mathematical, Physical and Engineering Science*, 464(2093):1181–1201, 2008.

[4] R. J. Asaro. Crystal plasticity. *Journal of Applied Mechanics*, 50:921 – 934, 1983.

[5] J. R. Asay and L. C. Chhabildas. Paradigms and challenges in shock wave research. In Y. Horie, L. Davison, and N. N. Thadhani, editors, *High-Pressure Shock Compression of Solids VI: Old Paradigms and New Challenges*, pages 57 – 119. Springer, New York, 2003.

[6] W. Band and G. E. Duvall. Physical nature of shock propagation. *American Journal of Physics*, 29(11):780–785, 1961.

[7] G. Bao and Z. Lin. High strain rate deformation in particle reinforced metal matrix composites. *Acta Materialia*, 44(3):1011 – 1019, 1996.

[8] L. M. Barker. A model for stress wave propagation in composite materials. *Journal of Composite Materials*, 5(2):140 – 162, 1971.

[9] Z. P. Bažant and T. B. Belytschko. Wave propagation in a strain-softening bar: Exact solution. *Journal of Engineering Mechanics*, 111(3):381–389, 1985.

[10] H. J. Böhm, A. Eckschlager, and W. Han. Multi-inclusion unit cell models for metal matrix composites with randomly oriented discontinuous reinforcements. *Computational Materials Science*, 25(1–2):42 – 53, 2002.

[11] S. Bonnan, P.-L. Hereil, and F. Collombet. Experimental characterization of quasi static and shock wave behavior of porous aluminum. *Journal of Applied Physics*, 83(11):5741–5749, 1998.

[12] N. Carrere, R. Valle, T. Bretheau, and J. L. Chaboche. Multiscale analysis of the transverse properties of ti-based matrix composites reinforced by SiC fibers: from the grain scale to the macroscopic scale. *International Journal of Plasticity*, 20(4–5):783 – 810, 2004.

[13] M. M. Carroll and A. C. Holt. Static and dynamic pore-collapse relations for ductile porous materials. *Journal of Applied Physics*, 43(4):1626–1636, 1972.

[14] N. Chawla and K. Chawla. Metal-matrix composites in ground transportation. *JOM Journal of the Minerals, Metals and Materials Society*, 58:67 – 70, 2006.

[15] N. Chawla, B. V. Patel, M. Koopman, K. K. Chawla, R. Saha, B. R. Patterson, E. R. Fuller, and S. A. Langer. Microstructure-based simulation of thermomechanical behavior of composite materials by object-oriented finite element analysis. *Materials Characterization*, 49(5):395 – 407, 2002.

[16] N. Chawla, R. S. Sidhu, and V. V. Ganesh. Three-dimensional visualization and microstructure-based modeling of deformation in particle-reinforced composites. *Acta Materialia*, 54(6):1541 – 1548, 2006.

[17] W. Chen and J. Fish. A dispersive model for wave propagation in periodic heterogeneous media based on homogenization with multiple spatial and temporal scales. *Journal of Applied Mechanics*, 68(2):153–161, 2001.

[18] Y. Chen and J. D. Lee. Determining material constants in micromorphic theory through phonon dispersion relations. *International Journal of Engineering Science*, 41(8):871–886, 2003.

[19] T. Christman, A. Needleman, S. Nutt, and S. Suresh. On microstructural evolution and micromechanical modelling of deformation of a whisker-reinforced metal-matrix composite. *Materials Science and Engineering: A*, 107:49 – 61, 1989.

[20] T. Christman, A. Needleman, and S. Suresh. An experimental and numerical study of deformation in metal-ceramic composites. *Acta Metallurgica*, 37(11):3029 – 3050, 1989.

[21] W. J. Clegg. A stress analysis of the tensile deformation of metal-matrix composites. *Acta Metallurgica*, 36(8):2141 – 2149, 1988.

[22] R. Dingreville, J. Robbins, and T. E Voth. Multiresolution modeling of the dynamic loading of metal matrix composites. *JOM*, 65(2):203–214, 2013.

[23] R. Dingreville, J. Robbins, and T. E. Voth. Wave propagation and dispersion in a nonlinear microstructured materials. *International Journal of Solids and Structures*, In preparation, 2013.

[24] T. J. A. Doel and P. Bowen. Tensile properties of particulate-reinforced metal matrix composites. *Composites Part A: Applied Science and Manufacturing*, 27(8):655 – 665, 1996.

[25] S.K. Dwivedi, J.R. Asay, , and Y.M. Gupta. Two-dimensional mesoscale simulations of quasielastic reloading and unloading in shock compressed aluminum. *Journal of Applied Physics*, 100, 2006.

[26] J. Engelbrecht, A. Berezovski, F. Pastrone, and M. Braun. Waves in microstructured materials and dispersion. *Philosophical Magazine*, 85(33–35):4127–4141, 2005.

[27] J. Engelbrecht and F. Pastrone. Waves in microstructured solids with nonlinearities in microscale. *Proceedings of the Estonian Academy of Sciences. Physics. Mathematics.*, 1:12 – 20, 2003.

[28] J. Engelbrecht, F. Pastrone, M. Braun, and A. Berezovski. Hierarchies of waves in nonclassical materials. In *Universality of Nonclassical Nonlinearity: Applications to Non-Destructive Evaluations and Ultrasonics*, pages 29–47. Springer, New York, 2006.

[29] A. C. Eringen. *Microcontinuum Field Theories: Foundations and Solids*. Springer, New York, 1999.

[30] A. C. Eringen. *Microcontinuum Field Theories: Foundations and Solids*. Springer, New York, 1999.

[31] A. C. Eringen and E. S. Suhubi. Nonlinear theory of simple microelastic solids. *International Journal of Engineering and Science*, 2:189–203, 1964.

[32] A. Evans, C. S. Marchi, and A. Mortensen. *Metal Matrix Composites in Industry: an introduction and a survey metal matrix composites*. Kluwer Academic Publishers, Dordrecht, the Netherlands, 2003.

[33] S. Forest and R. Sievert. Nonlinear microstrain theories. *International Journal of Solids and Structures*, 43(24):7224 – 7245, 2006.

[34] S. Forest and R. Sievert. Nonlinear microstrain theories. *International Journal of Solids and Structures*, 43(24):7224–7245, 2006.

[35] P. Fredriksson, P. Gudmundson, and L. P. Mikkelsen. Finite element implementation and numerical issues of strain gradient plasticity with application to metal matrix composites. *International Journal of Solids and Structures*, 46(22–23):3977 – 3987, 2009.

[36] M. D. Furnish, L. C. Chhabildas, W. D. Reinhart, W. M. Trott, and T. J. Vogler. Determination and interpretation of statistics of spatially resolved waveforms in spalled tantalum from 7 to 13 GPa. *International Journal of Plasticity*, 25(4):587–602, 2009.

[37] M. D. Furnish, L. C. Chhabildas, W. D. Reinhart, W. M. Trott, and T. J. Vogler. Determination and interpretation of statistics of spatially resolved waveforms in spalled tantalum from 7 to 13 GPa. *International Journal of Plasticity*, 25:587 – 602, 2009.

[38] P. Germain. The method of virtual power in continuum mechanics. part 2: Microstructure. *SIAM Journal on Applied Mathematics*, 25:556 – 575, 1973.

[39] P. Germain. The method of virtual power in continuum mechanics. Part 2: Microstructure. *SIAM Journal on Applied Mathematics*, 25:556 – 575, 1973.

[40] S. Gonella, M. S. Greene, and W. K. Liu. Characterization of heterogeneous solids via wave methods in computational microelasticity. *Journal of the Mechanics and Physics of Solids*, 59:959 – 974, 2011.

[41] S. Gopalakrishnan, M. Ruzzene, and S. Hanagud. *Computational Techniques for Structural Health Monitoring*. Springer Series in Reliability Engineering. Springer, 2011.

[42] D. Grady. Scattering as a mechanism for structured shock waves in metals. *Journal of the Mechanics and Physics of Solids*, 46(10):2017 – 2032, 1998.

[43] D. Grady. Scattering as a mechanism for structured shock waves in metals. *Journal of the Mechanics and Physics of Solids*, 46(10):2017 – 2032, 1998.

[44] D. E. Grady. Strain-rate dependence of the effective viscosity under steady-wave shock compression. *Applied Physics Letters*, 38(10):825–826, 1981.

[45] D. E. Grady. Microstructural effects on wave propagation in solids. *International Journal of Engineering Science*, 22(8-10):1181 – 1186, 1984.

[46] D. E. Grady. Structured shock waves and the fourth-power law. *Journal of Applied Physics*, 107(1):013506, 2010.

[47] A. Granato and K. Lücke. Application of dislocation theory to internal friction phenomena at high frequencies. *Journal of Applied Physics*, 27(7):789–805, 1956.

[48] M. Grujicic, B. Pandurangan, W. C. Bell, C. F. Yen, and B. A. Cheeseman. Application of a dynamic-mixture shock-wave model to the metal - matrix composite materials. *Materials Science and Engineering: A*, 528(28):8187 – 8197, 2011.

[49] M. Güden and I. W. Hall. Dynamic properties of metal matrix composites: a comparative study. *Materials Science and Engineering: A*, 242(1–2):141 – 152, 1998.

[50] V. E. Gusev, W. Lauriks, and J. Thoen. Dispersion of nonlinearity, nonlinear dispersion, and absorption of sound in micro-inhomogeneous materials. *The Journal of the Acoustical Society of America*, 103(6):3216–3226, 1998.

[51] M. F. Hamilton and D. T. Blackstock. *Nonlinear Acoutics*. Academic Press, San Diego, 1998.

[52] R. Hill. Elastic properties of reinforced solids: Some theoretical principles. *Journal of the Mechanics and Physics of Solids*, 11(5):357 – 372, 1963.

[53] R. Hill. The essential structure of constitutive laws for metal composites and polycrystals. *Journal of the Mechanics and Physics of Solids*, 15(2):79 – 95, 1967.

[54] R. Hill and J. R. Rice. Constitutive analysis of elastic-plastic crystals at arbitrary strain. *Journal of the Mechanics and Physics of Solids*, 20:401 – 413, 1972.

[55] T. J. Holmquist and G. R. Johnson. Response of boron carbide subjected to high-velocity impact. *International Journal of Impact Engineering*, 35(8):742–752, 2008.

[56] S. I. Hong and G. T. Gray. Bounds and self-consistent estimates for creep of polycrystalline materials. *Proceedings of the Royal Society of London A*, 348:101 – 127, 1976.

[57] S. I. Hong and G. T. Gray. Dynamic mechanical response of a 1060 Al/Al_2O_3 composite. *Journal of Materials Science*, 29:2987 – 2992, 1994.

[58] I. A. Ibrahim, F. A. Mohamed, and E. J. Lavernia. Particulate reinforced metal matrix composites - a review. *Journal of Materials Science*, 26:1137 – 1156, 1991.

[59] A. Jeffrey. Nonlinear wave propagation. *Zeitschrift fuer angewandte Mathematik und Mechanik*, 58:38–56, 1978.

[60] G. R. Johnson and T. J. Holmquist. An improved computational constitutive model for brittle materials. In S. C. Schmidt, J. W. Shaner, G. A. Samara, and M. Ross, editors, *High Pressure Science and Technology–1993*, pages 1075 – 1081. AIP Press, New York, 1994.

[61] G. I. Kanel, M. F. Ivanov, and A. N. Parshikov. Computer simulation of the heterogeneous materials response to the impact loading. *International Journal of Impact Engineering*, 17(1-3):455 – 464, 1995. Hypervelocity Impact.

[62] J. Kevorkian and D. L. Bosley. Multiple-scale homogenization for weakly nonlinear conservation laws with rapid spatial fluctuations. *Studies in Applied Mathematics*, 101(2):127–183, 1998.

[63] T. A. Khraishi, L. Yan, and Y. L. Shen. Dynamic simulations of the interaction between dislocations and dilute particle concentrations in metal - matrix composites (MMCs). *International Journal of Plasticity*, 20(6):1039 – 1057, 2004.

[64] U. F. Kocks. Laws for work hardening and low temperature creep. *Transactions of the ASME: Journal of Engineering Materials and Technology*, 98:76 – 85, 1976.

[65] H. Kolsky. *Stress Waves in Solids*. Dovers Publications, New York, 1963.

[66] E. Kröner. Allgemeine kontinuumstheorie der versetzugnen und eigenspannungen. *Archive for Rational Mechanics and Analysis*, 4:273 – 334, 1960.

[67] E. H. Lee. Elastic-plastic deformation at finite strains. *Journal of Applied Mechanics*, 36:1 – 6, 1969.

[68] W.-S. Lee, C.-F. Lin, and G.-L. Xiea. Dynamic shear deformation and failure behaviour of pure polycrystalline tungsten. *Materials Science and Engineering: A*, 247(1–2):102–112, 1998.

[69] J. W. Leggoe, A. A. Mammoli, M. B. Bush, and X. Z. Hu. Finite element modelling of deformation in particulate reinforced metal matrix composites with random local microstructure variation. *Acta Materialia*, 46(17):6075 – 6088, 1998.

[70] J. J. Lewandowski, C. Liu, and W. H. Hunt Jr. Effects of matrix microstructure and particle distribution on fracture of an aluminum metal matrix composite. *Materials Science and Engineering: A*, 107:241 – 255, 1989.

[71] Y. Li and K. T. Ramesh. Influence of particle volume fraction, shape, and aspect ratio on the behavior of particle-reinforced metal - matrix composites at high rates of strain. *Acta Materialia*, 46(16):5633 – 5646, 1998.

[72] W. K. Liu, T. Belytschko, and A. Mani. Random field finite elements. *International Journal for Numerical Methods in Engineering*, 23:1831 – 1845, 1986.

[73] J. Llorca, A. Needleman, and S. Suresh. An analysis of the effects of matrix void growth on deformation and ductility in metal-ceramic composites. *Acta Metallurgica et Materialia*, 39(10):2317 – 2335, 1991.

[74] D.J. Lloyd. Aspects of fracture in particulate reinforced metal matrix composites. *Acta Metallurgica et Materialia*, 39(1):59 – 71, 1991.

[75] E. Love, G. Scovazzi, and W. J. Rider. Algorithmic properties of the midpoint predictor-corrector time integrator. Sandia Technical Report SAND2009-1127, Sandia National Laboratories, Albuquerque, NM, 2009.

[76] E. Love and M. K. Wong. Lagrangian continuum dynamics in ALEGRA. Sandia Technical Report SAND2007-8104, Sandia National Laboratories, Albuquerque, NM, 2007.

[77] W. P. Mason and H. J. McSkimin. Attenuation and scattering of high frequency sound waves in metals and glasses. *The Journal of the Acoustical Society of America*, 19(3):464–473, 1947.

[78] D. J. McClements, P. Fairley, and M. J. W. Povey. Comparison of effective medium and multiple-scattering theories of predicting the ultrasonic properties of dispersions. *The Journal of the Acoustical Society of America*, 87(5):2244–2246, 1990.

[79] C. McVeigh and W. K. Liu. Multiresolution modeling of ductile reinforced brittle composites. *Journal of the Mechanics and Physics of Solids*, 57(2):244 – 267, 2009.

[80] H. Mecking and U. F. Kocks. Kinetics of flow and strain hardening. *Acta Metallurgica*, 19(11):1865 – 1875, 1981.

[81] T. Meurer, J. Qu, and L. J. Jacobs. Wave propagation in nonlinear and hysteretic media - A numerical study. *International Journal of Solids and Structures*, 39(21–22):5585–5614, 2002.

[82] J. C. F. Millett, G. T. Gray III, and N. K. Bourne. Measurement of the shear strength of pure tungsten during one-dimensional shock loading. *Journal of Applied Physics*, 101(3):033520, 2007.

[83] R. D. Mindlin. Micro-structure in linear elasticity. *Archive for Rational Mechanics and Analysis*, 16(1):51 – 78, 1964.

[84] R. D. Mindlin. Micro-structure in linear elasticity. *Archive for Rational Mechanics and Analysis*, 16(1):51–78, 1964.

[85] D.B. Miracle. Metal Matrix Composites - From science to technological significance. *Composites Science and Technology*, 65(15–16):2526 – 2540, 2005.

[86] A. Mortensen and J. Llorca. Metal Matrix Composites. *Annual Review of Materials Research*, 40:243 – 270, 2010.

[87] D. E. Munson and R. J. Lawrence. Dynamic deformation of polycrystalline alumina. *Journal of Applied Physics*, 50(10):6272–6282, 1979.

[88] L. E. Murr and D. Kuhlmann-Wilsdorf. Experimental and theoretical observations on the relationship between dislocation cell size, dislocation density, residual hardness, peak pressure and pulse duration in shock-loaded nickel. *Acta Metallurgica*, 26(5):847–857, 1978.

[89] D. H. Niblett and J. Wilks. Dislocation Damping in Metals. *Advances in Physics*, 9(33):1–88, 1960.

[90] T. G. Nieh, J. Wadsworth, and T. Imai. A rheological view of high-strain-rate superplasticity in alloys and metal-matrix composites. *Scripta Metallurgica et Materialia*, 26:703 – 708, 1992.

[91] A. N. Norris. Finite-amplitude waves in solids. In *Hamilton, M. F., Blackstock, D. T., Nonlinear Acoustics*, pages 263–276. Academic Press, 1998.

[92] S. Papargyri-Beskou, D. Polyzos, and D. E. Beskos. Wave dispersion in gradient elastic solids and structures: A unified treatment. *International Journal of Solids and Structures*, 46:3751 – 3759, 2009.

[93] R. H. J. Peerlings, M. G. D. Geers, R. de Borst, and W. A. M. Brekelmans. A critical comparison of nonlocal and gradient-enhanced softening continua. *International Journal of Solids and Structures*, 38(44–45):7723–7746, 2001.

[94] W. Prager. An introduction to the mathematical theory of plasticity. *Journal of Applied Physics*, 18:375–383, 1947.

[95] W. Ramberg and W. R.. Osgood. Description of stress-strain curves by three parameters. Technical Report 500/R25/1943, National Advisory Committee for Aeronautics, Washington, D.C., Technical Note No. 902, 1943.

[96] H. E. Read and G. A. Hegemier. Strain softening of rock, soil and concrete – a review article. *Mechanics of Materials*, 3(4):271–294, 1984.

[97] J. R. Robbins, J. L. Ding, and Y. M. Gupta. Load spreading and penetration resistance of layered structures – a numerical study. *International Journal of Impact Engineering*, 30(6):593 – 615, 2004.

[98] F. Roters, P. Eisenlohr, T. R. Bieler, and D. Raabe. *Crystal Plasticity Finite Element Methods*. Wiley–VCH Verlag GmbH and Co. KGaA, 2010.

[99] J. Segurado, C. González, and J. Llorca. A numerical investigation of the effect of particle clustering on the mechanical properties of composites. *Acta Materialia*, 51(8):2355 – 2369, 2003.

[100] J. K. Shang and R. O. Ritchie. On the particle-size dependence of fatigue-crack propagation thresholds in SiC-particulate-reinforced aluminum-alloy composites: Role of crack closure and crack trapping. *Acta Metallurgica*, 37(8):2267 – 2278, 1989.

[101] L. J. Sluys, R. de Borst, and H.-B. Mühlaus. Wave propagation, localization and dispersion in gradient-dependent medium. *International Journal of Solids and Structures*, 30(9):1153–1171, 1993.

[102] F. E. Stanke and G. S. Kino. A unified theory for elastic wave propagation in polycrystalline materials. *The Journal of the Acoustical Society of America*, 75(3):665–681, 1984.

[103] A. Tasdemirci and I. W. Hall. Experimental and modeling studies of stress wave propagation in multilayer composite materials: Low modulus interlayer effects. *Journal of Composite Materials*, 39(11):981 – 1005, 2005.

[104] A. Tasdemirci and I. W. Hall. Experimental and modeling studies of stress wave propagation in multilayer composite materials: Low modulus interlayer effects. *Journal of Composite Materials*, 39(11):981–1005, 2005.

[105] T. R. Tauchert and A. N. Guzelsu. An experimental study of dispersion of stress waves in a fiber-reinforced composite. *Journal of Applied Mechanics*, 39(1):98–102, 1972.

[106] G. I. Taylor. Mechanism of plastic deformation of crystals. Part I – theoretical. *Proceedings of the Royal Society of London A*, 145(855):362 – 387, 1934.

[107] İsmail Tirtom, Mustafa Güden, and Hasan Yildiz. Simulation of the strain rate sensitive flow behavior of SiC-particulate reinforced aluminum metal matrix composites. *Computational Materials Science*, 42(4):570 – 578, 2008.

[108] R. J. Twiss and A. C. Eringen. Theory of mixtures for micromorphic materials–i : Balance laws. *International Journal of Engineering Science*, 9(10):1019 – 1044, 1971.

[109] R. J. Twiss and A. C. Eringen. Theory of mixtures for micromorphic materials-ii. elastic constitutive equations. *International Journal of Engineering Science*, 10(5):437 – 465, 1972.

[110] R. Vaziri, D. Delfosse, G. Pageau, and A. Poursartip. High-speed impact response of particulate metal matrix composite materials - An experimental and theoretical investigation. *International Journal of Impact Engineering*, 13(2):329 – 352, 1993.

[111] F. Vernerey, W. K. Liu, and B. Moran. Multi-scale micromorphic theory for hierarchical materials. *Journal of the Mechanics and Physics of Solids*, 55(12):2603 – 2651, 2007.

[112] F. Vernerey, W. K. Liu, and B. Moran. Multi-scale micromorphic theory for hierarchical materials. *Journal of the Mechanics and Physics of Solids*, 55:2603 – 2651, 2007.

[113] E. Voce. The relationship between stress and strain for homogeneous deformation. *Journal Institute of Metals*, 74:537–562, 1948.

[114] T. J. Vogler, W. M. Trott, W. D. Reinhart, C. S. Alexander, M. D. Furnish, M. D. Knudson, and L. C. Chhabildas. Using the line-VISAR to study multi-dimensional and mesoscale impact phenomena. *International Journal of Impact Engineering*, 35(12):1844–1852, 2008.

[115] Z.-P. Wang and C.T. Sun. Modeling micro-inertia in heterogeneous materials under dynamic loading. *Wave Motion*, 36:473 – 485, 2002.

[116] Ze-Ping Wang. Void-containing nonlinear materials subject to high-rate loading. *Journal of Applied Physics*, 11:7213 – 7227, 1997.

[117] P. C. Waterman and Rohn Truell. Multiple scattering of waves. *Journal of Mathematical Physics*, 2(4):512–537, 1961. Cited 438 times.

[118] J. J. Williams, Z. Flom, A. A. Amell, N. Chawla, X. Xiao, and F. De Carlo. Damage evolution in SiC particle reinforced al alloy matrix composites by X-ray synchrotron tomography. *Acta Materialia*, 58(18):6194 – 6205, 2010.

[119] L. Xiong and Y. Chen. Coarse-grained simulations of single-crystal silicon. *Modeling and Simulation in Materials Science and Engineering*, 17:1 – 17, 2009.

[120] Y. Xu, J. Zhang, Y. Bai, and M. A. Meyers. Shear localization in dynamic deformation: Microstructural evolution. *Metallurgical and Materials Transactions A*, 39(4):811–843, 2008.

[121] S. Yadav, D. R. Chichili, and K. T. Ramesh. The mechanical response of a 6061-T6 Al/Al_2O_3 metal matrix composite at high rates of deformation. *Acta Metallurgica et Materialia*, 43(12):4453 – 4464, 1995.

[122] K. Yano and Y. Horie. Discrete-element modeling of shock compression of polycrystalline copper. *Physical Review B*, 59(21):13672 – 13680, 1999.

[123] C. F. Ying and R. Truell. Scattering of a plane longitudinal wave by a spherical obstacle in an isotropically elastic solid. *Journal of Applied Physics*, 27(9):1086–1097, 1956.

[124] J. T. Zhang, L. S. Liu, P. C. Zhai, Z. Y. Fu, and Q. J. Zhang. The prediction of the dynamic responses of ceramic particle reinforced MMCs by using multi-particle computational micromechanical method. *Composites Science and Technology*, 67(13):2775 – 2785, 2007.

[125] S. Zhuang, G. Ravichandran, and D. E. Grady. An experimental investigation of shock wave propagation in periodically layered composites. *Journal of the Mechanics and Physics of Solids*, 51(2):245–265, 2003.

A Derivation of the fourth order equation of motion

From the elasticity theory, using equations (35) and (36), the macrostress, microstress and interactive force are defined as,

$$\sigma = \frac{\partial \mathscr{W}}{\partial u_x} = \bar{E}\varepsilon^{el} - \bar{A}_{0\mu}\chi^{el} \ , \tag{88a}$$

$$\mu = \frac{\partial \mathscr{W}}{\partial \chi_x} = E_\mu \chi_x^{el} \ , \tag{88b}$$

$$\eta = \frac{\partial \mathscr{W}}{\partial \chi} = -\bar{A}_{0\mu}\varepsilon^{el} + B_{0\mu}\chi^{el} \ , \tag{88c}$$

where,

$$\bar{E} = E_0 + 2A_{0\mu} + B_{0\mu} \ \text{ and } \ \bar{A}_{0\mu} = A_{0\mu} + B_{0\mu} \ . \tag{89}$$

Extracting the elastic deformations from (88) yields the kinematic expressions defined in equation (37). By substituting the macrostress given by equation (88a) and the microdeformation given by equation (88b) into the rate form of macroscopic balance equation (34) yields an expression for the microstress in rate form of the type,

$$\mu_t = \frac{\bar{E}E_\mu}{\bar{A}_{0\mu}}\left(v_{xx} - \rho\frac{E_0 + (h_0 - 1)\bar{E}}{E_0\bar{E}}v_{tt}\right) \ . \tag{90}$$

Combining equation (39b) with equation (90) gives an expression of the rate of microdeformation as a function of the velocity such that,

$$(\chi_x)_t = h_\mu \frac{\bar{E}}{\bar{A}_{0\mu}}\left(v_{xx} - \rho\frac{E_0 + (h_0 - 1)\bar{E}}{E_0\bar{E}}v_{tt}\right) \ . \tag{91}$$

Similarly, the rate of interactive force can be expressed as a function of the velocity such that,

$$(\eta_x)_t = -\rho\frac{\bar{A}_{0\mu}}{\bar{E}}v_{tt} + \frac{B_{0\mu}\bar{E}}{\bar{A}_{0\mu}}\left(1 - \frac{\bar{A}_{0\mu}^2}{B_{0\mu}\bar{E}}\right)\left(v_{xx} - \rho\frac{E_0 + (h_0 - 1)\bar{E}}{E_0\bar{E}}v_{tt}\right) \ . \tag{92}$$

Taking the spatial derivative of the microscopic balance equation (34) with respect to x and substituting the microdeformation, microstress and interactive force by equations (91), (90) and (92) respectively, leads to the one-dimensional wave equation:

$$\begin{aligned} &\frac{\rho}{\bar{E}}\frac{\bar{A}_{0\mu}^2}{B_{0\mu}\bar{E}}v_{tt} - \left(1 - \frac{\bar{A}_{0\mu}^2}{B_{0\mu}\bar{E}}\right)\left[v_{xx} - \rho\frac{E_0 + (h_0 - 1)\bar{E}}{E_0\bar{E}}v_{tt}\right] = \\ &\frac{I_\mu}{B_{0\mu}}h_\mu\left[v_{xx} - \rho\frac{E_0 + (h_0 - 1)\bar{E}}{E_0\bar{E}}v_{tt}\right]_{tt} - \frac{E_\mu}{B_{0\mu}}\left[v_{xx} - \rho\frac{E_0 + (h_0 - 1)\bar{E}}{E_0\bar{E}}v_{tt}\right]_{xx} \ . \end{aligned} \tag{93}$$

DISTRIBUTION:

1	MS 0747	Remi Dingreville, 6233
1	MS 1195	Michael Furnish, 1646
1	MS 1323	Thomas Voth, 1443
1	MS 1323	Joshua Robbins, 1443
1	MS 0899	Technical Library, 9536 (electronic copy)
1	MS 0359	D. Chavez, LDRD Office, 1911

Sandia National Laboratories